PYROMETRY

for

WIND TUNNEL CALIBRATION

L. Minassian.

ABSTRACT

HIGH TEMPERATURE PYROMETRY

FOR

WIND TUNNEL CALIBRATION

bу

L. Minassian

A thesis submitted to the Faculty of Graduate Studies and Research of McGill University in partial fulfilment of the requirements for the Degree of Master of Engineering.

A primary requirement in the operation of the McGill High Enthalpy Wind Tunnel is the monitoring of the temperature of air • entering the test section.

The aim of the present project is two-fold :-

- a) Tunnel calibration in terms of total temperatures for various heating rates and for various mass flow rates.
- b) Determination of a suitable method for measuring the tunnel total temperature on a routine basis.

Optical pyrometry was the basis of investigation. The temperature of a radiation target, inserted in the temperature section of the tunnel, was measured with an optical pyrometer. The results obtained were compared with those obtained by a thermocouple for the lower range of temperatures (below 1800°K). The similarity of results of the two series, justifies the reliance on the optical pyrometer alone for the higher range when temperatures as high as 3000°K are attained.

The reproducible results obtained with the optical pyrometer, enabled calibration of the total radiation pyrometer which has the advantage of recording results automatically.

HIGH TEMPERATURE PYROMETRY.

FOR

WIND TUNNEL CALIBRATION

bу

L. Minassian

Submitted to the Faculty of Graduate Studies and Research of McGill University in partial fulfilment of the requirements for the Degree of Master of Engineering

McGill University.

Montreal, July 1968.

SUMMARY

A primary requirement in the operation of the McGill High Enthalpy Wind Tunnel is the monitoring of the temperature of air entering the test section.

The aim of the present project is two-fold:-

- a) Tunnel calibration in terms of total temperatures for various heating rates and for various mass flow rates.
- b) Determination of a suitable method for measuring the tunnel total temperature on a routine basis.

Optical pyrometry was the basis of investigation. The temperature of a radiation target, inserted in the temperature section of the tunnel, was measured with an optical pyrometer. The results obtained were compared with those obtained by a thermocouple for the lower range of temperatures (below 1800° K). The similarity of results of the two series, justifies the reliance on the optical pyrometer alone for the higher range when temperatures as high as 3000° K are attained.

The reproducible results obtained with the optical pyrometer, enabled calibration of the total radiation pyrometer which has the advantage of recording results automatically.

<u>ACKNOWLEDGEMENTS</u>

The author is grateful to his research director, Professor J. M. Forde, for his guidance and advice which were of great importance to the project.

Especial thanks are due to Messrs. J. E. Kelly, A. M. Ahmed and G. B. Mackintosh for their assistance during the experiments as well as to Mr. R. C. Biggs for his help in the theoretical part; to Messrs. D. Bland and R. Camarero for their help in the diagrams and to Miss E. Bartley for the excellent job of typing the manuscript.

The financial support of the Defence Research Board of Canada is acknowledged.

TABLE OF CONTENTS

SUMMARY			(i)
ACKNOWLEDGEMENTS			(ii)
TABLE OF CONTENTS			(iii)
LIST OF SYMBOLS			(iv)
1.	INTRODUCTION		
2.	GENERAL CONSIDERATIONS		4
	2.1.	Material Applicability to High temperature Oxidizing Atmosphere	5
	2.2.	Black Body Simulation	7 .
	2.3.	Gas Radiation and Air dissociation	10
	2.4.	Radiation-Conduction Losses for Probes in Hot Air	12
3.	EQUIPMENT AND INSTRUMENTATION		16
	3.1.	Experimental Procedure	20
	3.2	Range of Investigation	22
4.	DISCUSSION		
·	4.1.	General Tunnel Performance	23
٠	4.2.	Analysis of Experimental Results	24
5.	CONCI	CONCLUSIONS	
	RECOMMENDATIONS		28
REFERENCES			29
APPENDICES			33
TABLES			47.
FIGURES			5.5

LIST OF SYMBOLS

a	cross-sectional area
A	surface area
E	emissivity
E _a (x)	emissivity along cylindrical wall of a cavity
EA	total air emissivity
E _w	water vapour emissivity
EbA	monochromatic emissive power of a black body
F	black body shape factor
チ	gray body shape factor
hc	heat transfer coefficient by forced convection
hr	heat transfer coefficient by radiation
K	thermal conductivity
K,	luminosity factor for monochromatic screen
M	mass flow rate
N _{u p}	Nusselt number based on diameter D
P	Perimeter
Pr	Prandtl number
PT	total air pressure
P _w	water vapour partial pressure
Q_c	heat transfer by convection
Q_{K}	heat transfer by conduction
$Q_{\mathbf{R}}$	heat transfer by radiation
R	gas constant
Re _D	Reynolds number based on diameter D

 ${\tt T}$ true temperature ${\tt t}_{\rm R}$ spectral transmission of optical pyrometer monochromatic screen ${\tt V}_{\rm T}$ total air volume ${\tt V}_{\rm w}$ water vapour volume ${\tt W}_{\rm T}$ total weight of air ${\tt W}_{\rm L}$ weight of water vapour

Greek Symbols

wavelength

effective wavelength at temperatureT

T1-T2 mean effective wavelength between temperatures T1 and T2

u one micron

reflectivity

Stefan-Boltzmann constant

T3 glass spectral transmissivity (fig. 39)

Subscripts

conditions at thermocouple or target supporting rods
a apparent value
conditions at geometric centre
conditions at thermocouple tip.
Gondition for air
mean value
ponditions at pebble bed
conditions at target

conditions at the wall.

1. INTRODUCTION

One of the basic tools used by the Hypersonic Propulsion

Laboratory of the Mechanical Engineering Department of McGill

University is a High Enthalpy Supersonic Wind Tunnel.

The total temperature of air is a primary parameter in controlling the Hot tunnel (HT-1) performance. Theoretical calculations, which were the basis for determining this temperature in the past, lead to inaccuracies due to the inevitable assumptions which must be made when theory is the only source of information (Appendix IV).

Because of the tunnel operating conditions, monitoring the temperature, which can attain 3000°K, presents considerable difficulty. It is, however, important that a routine method be devised to permit accurate total temperature monitoring during operation. The oxidizing atmosphere and high temperature preclude the use of thermocouples in the main stream except in those cases when the temperature does not exceed 1800°K. The problem then is to establish a permanent system which will permit accurate temperature monitoring with a minimum of interference to the test procedure.

Optical pyrometry appeared to be most promising and several methods based upon this approach, were considered of which two will be examined in detail.

The radiating wall of the temperature section may be viewed with an optical (monochromatic) pyrometer through a glass window. The problem is then reduced to correlating the wall temperature to

that of the free stream. This would be the preferred approach, if feasible, since it offers no obstruction to the air flow.

An alternate solution would be the permanent location of a radiation target at the geometric centre of the temperature section with some form of supporting system (Fig. 3). The pyrometer may then be focused on the target as well as on the wall. The true air temperature at the target may be determined by applying the appropriate corrections made necessary due to heat lost by conduction and radiation to the surrounding wall. For the lower range of temperatures, (below 1800° K), a very accurate traversing thermocouple would be used together with the optical pyrometer. Comparison of the results obtained by the two instruments would establish the necessary corrections to justify the use of the optical pyrometer alone at elevated temperatures when thermocouples fail.

Various additional corrections were considered such as effects of glass transmission and gas radiation as shown in Appendices I and III; Figure 4 shows these radiating (or absorbing) mediums between the pyrometer and the radiating wall.

The type of instruments to be used are restricted to those existing in the laboratory. The particular procedure applied must give rapid response since test runs are limited to short periods to prevent overheating of the various tunnel components (see Section 3.1).

The following assumptions are made :-

- Axisymmetric flow.
- 2) Diffuse gray body existence in temperature section.

- 3) Black body emission from radiation target, and wall enclosure (See Section 2.2).
- 4) Uniform target temperature at steady state.

 The turbulent nature of the flow field

 (Appendix V) justifies this assumption. The radiation target is located centrally in the turbulent core where the air temperature may be assumed constant for the range of Prandtl Numbers (0.7 0.8) and Reynolds Numbers

 (12,000 30,000) considered (Ref. 44).
- 5) Uniform wall temperature at steady state.
- 6) Negligible gas radiation (Appendix I).
- 7) Zero pressure gradients in a transverse direction to the air flow.
- 8) Zero spectral emission by pyrex glass (Appendix III).
- 9) Neglect errors less than 1%.

2. GENERAL CONSIDERATIONS

During the experimental stage of the project, readings were taken only in the section upstream of the supersonic nozzle where the flow is subsonic. Figure 2 shows the location of this section in relation to the nozzle and pebble furnace.

The use of wall temperature alone to determine the free stream temperature by means of some form of correlation appears to be an ideal solution as it involves no insertion of probes in the temperature section. The correlation at high temperatures must be determined in conjunction with a radiation target located at the geometric centre of the temperature section. The target to be dispensed with after the appropriate correlation is established.

The relationship between free stream and wall temperature would have the following form

$$T_c = f(T_w, T_p, M, Re_D, Pr, Q_L)$$
 2.0

where Q_L = Heat lost to atmosphere by conduction through the wall as air travels from the pebble furnace to the temperature section (Fig. 2).

Several problems, however, arise in formulating equation 2.0. Due to the allowable running times (Section 3.1) only a very limited number of mass flow rates may be obtained for any one pebble bed temperature; accurate measurements and control of the latter is very difficult with the existing tunnel conditions (see Section 4.2). Q_L is unknown and may only be assumed approximately. Finally, the flow is not fully developed at the section and there is a region of vorticity due to a sudden enlargement

of the section diameter (Figure 34) causing irreproducible results.

A plan view of the temperature section is shown in Figure 3 with the nozzle removed and a general view is shown in Figure 3a with the nozzle at its proper location.

2.1 Material Applicability To High Temperature.

Oxidizing Atmospheres

Two major factors are involved in so far as the size of the radiation target is concerned:-

- a) minimum flow disturbance.
- b) minimum mass to shorten the time required for steady state prevalence.

Target minimum size is limited to 3/8 inch diameter by the available optical pyrometer; a rectangular piece $1/2 \times 1/2 \times 3/4$ inch was used (Figure 5c) with two 3/8 inch diameter cylindrical supports.

The rectangular shape of the target was unavoidable because of machining problems (Section 3). The factors controlling the choice of target material were the following:-

- melting point
- 2) resistance to oxidation
- 3) surface emissivity (Spectral and total normal)
- 4) thermal conductivity
- 5) density
- 6) resistance to thermal shocks

The contradicting nature of items 1 and 6 was a major difficulty. High temperature materials are in general poor thermal conductors and steep temperature gradients are liable to be set up

resulting in high internal stresses and finally mechanical failures.

Campbell (Ref. 5) gives a concise accurate discussion of high temperature materials used in oxidizing atmospheres, the advantages and disadvantages of which are shown in Table (1) (P. 47). The use of Alumina coated graphite in past experiments conducted at the Hypersonic Propulsion Laboratories indicated the unreliability of this material because of the Alumina cracking with subsequent material deterioration.

Table (1) suggests carbides and cermets as appropriate materials with promising properties; the latter being still in the development stage, carbides were selected as target material.

The first experiments were carried out with tungsten carbide (WC) for both target and supporting rods (Figure 6a). The rapid formation of a green scale over the target at 1800°K - 2000°K with subsequent material deterioration was the major drawback. The scale was powdered and examined by X-ray diffraction technique; it was found to be predominantly tungsten trioxide (WO₃) with some unidentified materials, presumably Zirconium Oxide.

A cylindrical (1 inch diameter x 1 inch long) Silicon carbide target (Figure 6b) was next used. No appreciable oxidation was detected but its relatively high density created a problem; the time taken for the target to reach steady state was considerably longer than the allowable running periods (Section 3.1). The low thermal conductivity of SiC (3.17 BTU hr. -1 ft. -20 f -1 ft.) caused steep temperature gradients in the direction of air flow (Figure 6c) and a thermal shock which eventually led to mechanical failure.

When a specially prepared Silicon Carbide foam was used, excellent results were obtained. Its applicability to the experiment was largely attributed to its low density and high porosity which permitted rapid attainment of steady conditions. However, the limited quantity of this material available necessitated the use of a specially prepared sintered boride no. 6 (Ref. 7) also with satisfactory results.

A newly developed product, Cellulose Carbon was suggested (Ref. 22) but could not be obtained. It is an encouraging material with a very high melting point (over 3500°K). Table (2) gives, in a summarized form, material applicability as radiation targets in order of preference.

2.2 Black Body Simulation

Several methods are available to determine the true temperatures of radiating bodies. Apparent temperature measurement of non black bodies with subsequent correction (Ref. 8) is one approach while creation of black body emission followed by true temperature measurement is another.

The latter approach was adopted primarily because of inadequate information on material spectral emissivity at elevated temperatures.

Figures 8 and 9 show the distribution of normal spectral emissivity (0.665 μ) of SiC and Zirconia respectively (Ref. 9) against temperature for a range of temperatures 1360°F to 2900°F, while Figure 11 gives the variation with wavelength at 1243°K with an additional table to account for temperature variation. No

information is available above 1800°K. The situation is identical with other materials.

The classical example of black body emission from gray bodies will be followed by considering radiation emitted from a hollow space (Ref. 11). The test section agrees very well with this situation (Fig. 10a), when measuring wall temperatures; the existence of a gray body (radiation target), however, within the enclosure, having a different temperature from the surrounding wall, may appear as a deviation from black body radiation.

It may be shown that the total intensity of radiation leaving this non-black body will be the same as that emitted by a black body. This may be explained by the following relation for an opaque gray body:

$$E + R = 1$$
 2.1

where E = emissivity of body

R = reflectivity of body

The target emits radiant energy of lower intensity than a black body but at the same time reflects part of the energy falling upon it from the walls of the enclosure; the final effect is an equivalent black body radiation leaving the enclosure.

Lest the above reasoning appear crude, a further step was taken to ensure black body emission. This was done by opening a cylindrical cavity (Figure 10b) in the non-black body to improve the emissivity characteristic of the material. A detailed analysis of this phenomenon for gray, diffuse surfaces is dealt with by Buckley (Ref. 12) and Sparrow (Ref. 13), while the experimental verification is undertaken by Vollmer (Ref. 14). The more accurate analysis of Sparrow will be outlined.

A radiant flux balance within finite length cavities results in a pair of simultaneous integral equations, the solutions of which are carried out numerically for different values of $\frac{L}{d}$ (L is cavity depth, d is cavity diameter) ranging from 4.0 to 0.25, (Figure 10c); three different materials are used with emissivities 0.9, 0.75 and 0.5. Consideration is given to variation of radiant flux (radiosity) leaving the ciruclar disc which closes the end of the cavity (Figure 10c) at x = L; Buckley (Ref. 12) on the other hand assumes constant flux in that region. The results are shown in Figure 12 (a, b, and c) for construction materials of emissivities 0.9, 0.5 and 0.75 respectively. The distribution of apparent or effective emissivity over the surfaces of a hole with a particular $\frac{L}{d}$ is given by a discontinuous curve composed of two parts. Upward sloping curves give variations of $E_a(x)$ along the cylindrical wall, while downward sloping curves $(E_a(r))$ give variations along the radius of the circular disc at the end of the hole. The latter curve which carries its own scale is of interest, as optical devices are focused on this surface. The total normal emissivities of Silicon-Carbide foam (Ref. 9) and Sintered Boride No. 6, vary between 0.7 and 0.85 (Figures 13, 14). Figure 12c then applies for the two materials and particularly the curve $\frac{L}{d} = 1$, Table 3 (Page 49) shows these results in (d = cavity diameter). convenient form.

The improved effective emissivity of 0.9389 - 0.9553 (Table 3) for the end disc together with the previous reasoning of emission from hollow spaces justify the final assumption of black body prevalence as sensed by the pyrometer. The example

in Appendix II illustrates the error magnitude resulting from assuming black body radiant emission from gray targets.

2.3 Gas Radiation and Air Dissociation

The unquestionable transparence of all radiant gases in the visible range of the spectrum is a vital point when considering the optical (Monochromatic, 0.663μ) pyrometer's readings. It is this insensivity to gas radiation that places it at a higher level of accuracy when compared to the total radiation pyrometer.

For the range of temperatures under consideration, heterpolar gases have emission bands of sufficient magnitude to merit consideration; some of these are hydrocarbons, sulphur dioxide, ammonia, hydrogen, carbon monoxide and water vapour, the last two being the dominant ones. Above 3000°K, however, polyatomic gases are seldom met with, due to dissociation, but diatomic molecules dominate; thus air, for example, will radiate between 3000°K and 10,000°K as a result of NO formation (Refs. 15 and 16). On the other hand, gases or gas mixtures with symmetrical molecules like 02, H2, N2 are practically transparent to thermal radiation.

Figure 15 (Refs. 17 - 20) illustrates the main distinction between solids and gases; with the former, the distribution of intensity of radiation against wavelength is continuous while with the latter it is essentially discontinuous consisting of a few narrow bands scattered over the infrared spectrum.

The emission bands of water vapour are of interest to the present project, since H₂O vapour is formed from the products of combustion of the afterburner (Ref. 35); the intermittent

presence of water droplets on the glass windows of the temperature section was very noticeable.

Figure 16 illustrates the emission bands of ${\rm H}_2{\rm O}$ vapour for various layers of gas and its effect on the total radiation pyrometer readings is given in Appendix I.

The phenomenon of dissociation is a very remote possiblity for the range of air temperatures and pressures investigated. Figure 17 indicates the temperatures and pressures at which dissociation becomes noticeable, the ordinate Z* being the degree of dissociation. At a pressure of 10 atm. (this is higher than the pressure attained during the experiments), air dissociates at 3000°K, while below this it is considered as an ideal gas. The purpose of considering the effects of dissociation on the experiment is solely for the future when temepratures over 3000°K will be attained.

Detailed analysis of dissociation with relevant chemical reactions have been treated in References 28 and 29, while Reference 41 gives tables of thermodynamic properties in chemical equilibrium for partially or fully dissociated air (and for ionized air if the temperature is high enough), which is treated as a mixture of real gases.

Direct effects of dissociation on optical temperature measurements may be summarized as follows:-

- A) Formation of NO at temperatures over 3000°K, causes emission bands, overlapping with those of the radiation target.
- B) Deviation of thermodynamic properties of the

dissociated air from an ideal gas has to be taken into account when applying the necessary temperature corrections of Section 2.4.

2.4 Radiation - Conduction Losses for Probes and Targets in Hot Air

The ultimate aim of determining air temperature, using the two basic instruments, viz. Thermocouple and Optical pyrometer, requires corrections for the heat lost to the surrounding enclosure; both instruments measure apparent air temperature. The thermocouple reading is that of its tip while the optical pyrometer essentially reads the target temperature. Figure 18 illustrates this sequence in the form of a flow chart.

A. <u>Thermocouple Correction</u>

For an element of the probe $\S x$ long at a distance x from the tip (Figure 19a), there is the following relation at steady state:-

(a)

Heat gained by forced Convection ($\S Q_c$)

(b)

+ Heat gained by gas radiation

(c)

= Heat lost to enclosure wall by Conduction ($\{\zeta_{ij}\}$

(d)

+ Heat lost to enclosure wall by Radiation (Q_p) 2.2

The case is essentially an extended surface with uniform cross-section and no temperature gradients in the direction of gas flow. The second term (b) in the L.H.S. of equation 2.2 will be neglected (Assumption 6, Section 1). The second reason for neglecting gas radiation is the fact that transparent gases produce larger errors in temperature measurements than opaque gases. The case of larger errors is thus treated.

Equation 2.2 is reduced to :-

but $SQ_c = h_c P(T_G - T) Sx$ 2.4

where T = probe temperature at distance xfrom tip (Figure 19a).

and
$$SQ_{K} = -Ka \frac{d^{2}T}{dx^{2}} Sx^{*}$$
 2.5
 $SQ_{R} = hr (T-Tw) PSx$ 2.6

where hr = heat transfer coefficient by radiation which is assumed constant (Appendix V); substitute in equation 2.3 and rearrange

$$-\frac{d^{2}T}{dx^{2}} + n^{2}T = m^{2}T_{G} + (n^{2} - m^{2})T_{W} \dots 2.7$$

$$m^{2} = \frac{h_{c}P}{Ka} \qquad d \qquad n^{2} = \frac{(h_{c} + h_{r})P}{Ka}$$

* the -ve sign indicates that for +ve x and +ve $\frac{dT}{dx}$, the net outflow of heat from the element g_x is negative, viz. net inflow, (Appendix VII, p. 46).

B. Correction for Optical Pyrometer Reading

Equation 2.7 also applies for a heat balance of the supporting rod (Figure 19b) with

$$m^2 = \frac{\bar{h}_c \bar{P}}{\bar{K} \bar{a}}$$
, $n^2 = \frac{(\bar{h}_c + \bar{h}_r) \bar{P}}{\bar{K} \bar{a}}$

The bars indicate values relevant to the tungsten Carbide (WC) supporting rod.

Boundary Conditions

A. Thermocouples

1.
$$a = b$$
 $T = Tw$ (Figure 19a)

2.
$$extit{e$$

B. Optical Pyrometer

1.
$$ax = L$$
 $T = Tw$ (Figure 19b)

2.
$$a = 0$$
 $\frac{dT}{dx} = 0$ (Figure 19b)

The rod is in firm contact with the radiation target resulting in a zero temperature gradient there. (The target itself is at uniform temperature by assumption 4 of Section 1.)

Substituting the boundary conditions in Equation 2.7 and solving

A. For Thermocouple

B. For Optical Pyrometer

$$T_G = T_W + (T_T - T_W) \left(\frac{\overline{h_c} + \overline{h_r}}{\overline{h_c}} \right) \frac{\cosh nL}{\cosh nL - 1} \dots 2.9$$

Equations 2.8 and 2.9 show:-

- a) Knowing thermocouple reading and wall temperature, air temperature may be determined at the location of the tip, for each flow rate.
- b) Knowing target and wall temperatures, air temperature may be determined for each mass flow rate at the location of the target, viz. geometric centre of the test section.

A discussion of properties and flow parameters in connection with Equations 2.8 and 2.9 is given in Appendix V, and a specific example is solved in Appendix VI.

3. EQUIPMENT AND INSTRUMENTATION

Various techniques were examined prior to the final decision on the choice of instruments. The particular measuring instruments used were selected from equipment available in the laboratory, consideration being given to the ease with which these could be adapted to the experiment.

A. <u>Temperature Section</u>

Figure 20 indicates the section with the appropriate locations of instruments used. One major difficulty encountered during the experimental stage was due to the temperature section position relative to the location of the zirconia pebbles (Figure 2). There was intermittent ejection of zirconia pebble segments which tended to damage any probe inserted.

B. Radiation Target

Only a limited quantity of Silicon Carbide foam was available, hence the use of Sintered Boride No. 6; the manufacturer (Ref. 7) had discontinued the production of the former. Machining difficulty was the sole reason for choosing rectangular shapes; Silicon Carbide foam was an extremely brittle material while Sintered Boride No. 6 was very hard and required spark erosion as a cutting process.

C. Thermocouples

The Platinum Vs. Platinum - 10% Rhodium thermocouple used, is useful in determining the test section temperature profile. It can be used intermittently up to 1900° K. Its major drawback is

the excessive grain growth above 1600°K when it is used for prolonged periods; this weakens the platinum element causing fracture eventually. Because of the short allowable running periods for each furnace condition, the use of protecting tubes had to be avoided since these decreased the thermocouple's response speed considerably. Refractory metals used for ultra high temperature thermocouples have been considered in the past but no positive results have appeared as yet (Ref. 2.)

Figure 21 indicates the five locations of the traversing thermocouple (Standard Pt Vs Pt - 10% Rhodium). The calibration of the wall thermocouple was undertaken in a controlled electric furnace (figure 22).

D. Optical (Monochromatic) Pyrometer

The excellent performance of optical (monochromatic) pyrometers as opposed to the inadequate and inaccurate measurements of thermocouples at elevated temperatures, was the primary reason for using the former. The dependence of the disappearing filament type pyrometer on spectral emissivity of the material on which it is focused, was avoided by simulating black body conditions, (Section 2.2).

Specifications

Type: Disappearing Filament (8622)

Adjustable focus

Accuracy: + 1%

Range: Low 1400° - 2250°F

 $(760^{\circ} - 1232^{\circ}C)$

The instrument was calibrated on 25th May, 1962, by the N.R.C. The provision of a range extension screen, increased the higher limit of 5200°F by reducing the intensity of light coming from the heated object. Figure 23 indicates the effect of using this absorption screen with the low range scale of the instrument. The one per cent accuracy as specified by the manufacturer (Ref. 40) was the basis for assumption 9 (Section 1.)

The monochromatic screen used in the form of red glass is not as absolutely monochromatic as the name implies; it has a definite width of wavelengths at which transmission takes place. This is illustrated in Figure 24 for the type of red glass (F-4512) used (Ref. 40); hence the definition of mean effective wavelength for a finite temperature interval. This is the wavelength for which the relative brightness as calculated from Wien's equation for the given temperature interval, is the same as the ratio of the integral luminosities measured through the red screen. Thus

$$\frac{\int_{0}^{\infty} E_{bA}(T_{1}) f_{R} K_{A} dA}{\int_{0}^{\infty} E_{bA}(T_{2}) f_{R} K_{A} dA} = \left[\frac{E_{bA}(T_{1})}{E_{bA}(T_{2})}\right] \frac{1}{T_{1}-T_{2}}$$

t_R is given in Figure 24, $A_{1}-T_{2}$ is determined from

Equation 3.1 using a step by step integration. For the type of red glass used viz. Jena "Rotfilter" No. F-4512, the authors of

Reference 38 have calculated the mean effective wavelength for various temperature intervals as shown in Table 4 (a) (Page 50).

Of interest is the effective wavelength for a particular temperature rather than the mean effective wavelength for an interval of temperatures. The effective wavelength (λ_{T}) may be defined as

$$\frac{1}{\lambda_{T}} = \lim_{\substack{T_{2} \to T \\ T_{1} \to T}} \frac{1}{\lambda_{T_{1} - T_{2}}}$$
(Ref. 21)

The importance of determining the effective wavelength arises from black body conditions when both brightness and colour temperatures approach the true black body temperature. Reference 38 gives the value for various temperatures (Table 4 (b) (Page 50.)) The surprisingly small variation in effective wavelength for a range 1300° - 3100° K, justifies the use of a constant mean value of 0.6633 with Equation A.3.1. (Appendix III).

E. Total Radiation Pyrometer

Specifications

Type: Brown Radiamatic

Assembly No.: 75505-5

Lens No.: 75522-2

Lens Types: Fused Silica Glass

Wavelength Sensitivity: $0.3 - 3.8 \mu$

The dependence of the instrument on the focused surface area was a major issue. The calibration curves (Figure 35 a and b) show that for a certain temperature, the millivolt output of the pyrometer is greater with larger diameters (3/4 inch for Target window), than with smaller diameters (1/4 inch for wall window.)

F. Pitot Tube

A stainless steel pitot tube with graphite lined tip
was used to determine the velocity gradient across the test section.
High temperature zirconia pebble ejection, however, damaged this
instrument in a few runs.

G. Static Pressure

Pressure tapping at the wall, indicated the static pressure by using strain gauge pressure transducers.

H. Visicorder

A Honeywell Brown Heiland Visicorder was used as a direct recording instrument. Four channels were used simultaneously for the following:

- 1. Section static pressure
- 2. Traversing thermocouple
- 3. Wall thermocouple
- 4. Total radiation pyrometer

I. Main Air Supply Orifice

A Square edge type of orifice plate is used for mass flow rate calculations; a graph is provided (Ref. 39) for standard air inlet conditions of 115 psia and 520°R with an additional correction factor distribution for deviations from standard.

3.1 <u>Experimental Procedure</u>

Time was the main element in choosing a particular procedure, most applicable to the existing situation. Prolonged subjection of tunnel components and specifically the supersonic

nozzle, to the upper limit of temperatures, could not be tolerated.

A maximum of 8 minutes was taken as the standard period allowable for each pebble bed temperature for a series of operating conditions; the steps followed were thus repeated for various pebble bed temperatures on different days.

A. <u>Heating Cycle</u>

See Reference 1.

B. Blowdown Cycle

At steady state :-

- 1. Measure mass flow
- a) Traverse the thermocouple forward from wall to target (Figure 20)
 - b) Measure target temperature with the optical pyrometer while the visicorder records wall temperature through the total radiation pyrometer. Switch locations of two pyrometers and measure the wall temperature with the optical pyrometer while the visicorder records target temperature through the total radiation pyrometer.

Note: Steps 2 (a) and 2 (b) are taken simultaneously.

- 3. a) Operate the afterburner
 - b) Allow time for steady state prevalence
- 4. Repeat steps 1 and 2 (a and b)
- 5. Change air mass flow rate
- 6. Allow time for steady state prevalence

- 7. Repeat steps 1 and 2, (a, b)
- 8. a) Shut off the afterburner
 - b) Allow time for steady state prevalence.
- 9. Repeat steps 1 and 2 (a, b).
 Continue the process for 8 minutes.

3.2 Range of Investigation

Table 5 indicates the ranges of air pressure, mass flow rates and total temperatures investigated during the experiment together with factors governing the upper and lower limits.

4. DISCUSSION

4.1 General Tunnel Performance

The purpose of the experiments, carried out in this project, was primarily to set up a procedure to monitor total temperatures accurately. During the process of investigation, however, some additional tunnel characteristics were revealed; these are outlined below:-

The zirconia pebble bed which acted as the heat source during the blowdown cycle, proved to be very efficient in this respect. This is illustrated in Figure 25 (a and b) which shows the readings of the traversing thermocouple. For all the cases considered, the temperature remained constant for the entire running period of 8 minutes once steady state had been reached.

The time required for the thermocouple to reach steady state depends on pebble bed temperature and mass flow rate. Figure 25a shows the response for two different mass flows at the start of blowdown while Figure 25b shows the response at later stages.

The wall behaviour was identical with that of the thermocouple but the major drawback was the greater time taken to reach steady state. Figures 26 and 27 illustrate this behaviour as measured with a wall thermocouple embedded inside the wall. Each figure shows the response for a particular pebble bed temperature subjected to various conditions of mass flow rate with or without the afterburner. Similar responses were experienced for the entire set of runs and may thus be

summarized by stating that approximately 150 seconds are required to reach steady state at the start of blowdown and only 90 seconds whenever the flow rate is changed or when the afterburner is put into operation or shut off.

The maximum air velocities attained during the experiments were less than 60 ft/sec; at such velocities the dynamic temperature becomes negligible in comparison to the static temperature, the latter being always over 1000°F. The air temperatures determined in the following section may thus be considered as total temperatures.

4.2 <u>Analysis of Experimental Results</u>

The readings of the traversing thermocouple and optical pyrometer are shown in table 8 for various pebble bed temperatures and mass flow rates. The first column designated for run numbers, has three figures A B C. "C" indicates a certain pebble bed temperature. "B" has two conditions: - 1) for operation without the afterburner, 2) for operation with the afterburner. "A" indicates mass flow conditions.

The mass flows of $\rm H_2$ and $\rm O_2$ injected during afterburner operation, were 0.000465 and 0.0066 lbs/sec respectively and may be neglected in comparison to the main air flow, which was 0.1 - 0.2 lbs/sec.

The pebble bed temperature was determined with the optical pyrometer as viewed from the nozzle 1/4 inch diameter throat; the readings are approximate due to the presence of the target between the pebble bed and the instrument, thus decreasing the effective focused area; in most cases part of the surrounding

wall was focused as well. The general view as seen with the instruments is shown in Figure 28. The pebble bed temperatures were therefore taken to be accurate to $\frac{+}{25}$ of the measured value.

Figures 29 - 33 indicate true air temperature profiles after the relevant corrections are applied to the readings of table 8. Each figure represents one pebble bed condition at various mass flow rates. Part "a" is for operation without the afterburner, while part "b" is for operation with the afterburner. The two extreme points, viz. wall and geometric centre, were determined with the optical pyrometer, and the intermediate points with the traversing thermocouple. Originally it was intended to have as many mass flow rates as possible for each pebble bed temperature; figure 29 is the best in this respect with 3 flows, whereas figure 33 is the worst with one flow rate, the main reason for this limitation being the short allowable running times (Section 3.1).

For the range of temperatures and mass flows considered, figures 29 and 30 show that for normal operation the higher the mass flow rate, the nearer is the air temperature to that of the pebble bed; above 0.1495 lbs/sec (Figure 29) however, no appreciable increase is noticed in temperature, indicating that there is an optimum flow rate at which the air leaves the pebbles with maximum heat transfer. The difference between air and pebble bed temperature may also be attributed partly to heat lost to the surroundings as it travels 24 inches from the pebbles to the test section. The sharp increase in air temperature with afterburner operation is seen to

vary 200°K - 450°K (Figures 29 - 32) depending on the mass flow rate and pebble bed temperature. The increased gradients at the geometric centre for parts "b" (with afterburner), are attributed to the afterburner flame which tends to heat the main air stream in a non-uniform manner.

The presence of an inflexion point in Figures 29 - 33, is due to a vortex system resulting from the enlargement of section diameter (Fig. 34). The region most influenced by this vortex system is location 1 (Fig. 21) where there tends to be a dead region and hence low temperatures.

The radiation pyrometer output versus temperature is shown in Figure 35 (a and b); the calibration was undertaken with the help of the optical pyrometer. The instrument is calibrated for a circular surface 1/4 inch diameter at the wall and 3/4 inch diameter at the radiation target; the sensitivity of the pyrometer to the focused surface area was the reason for separate calibrations.

5. CONCLUSIONS

Total air temperatures have been monitored during operation of the McGill High Enthalpy Wind Tunnel, by introducing a radiation target in the temperature section; the radiation emitted, as measured with an optical (monochromatic) pyrometer, was taken to be the criterion for its temperature at thermal equilibrium.

True air temperature has been determined from the target temperature by applying the relevant corrections made necessary due to heat lost by conduction and radiation to the surroundings.

The original intention of correlating the section wall

temperature to that of free stream had to be discarded because of
several independent parameters some of which could not be measured
accurately; the important parameters were flow rate, Reynolds
number, pebble bed temperature and heat lost to the atmosphere
as air travels from the pebble furnace to the temperature section.

Maximum air temperature attained was 2200°K when the pebble bed temperature was 1800°K. Higher temperatures may be attained by increasing either or both the pebble bed temperature and hydrogen mass injected through the afterburner.

The procedure developed will allow a continuous monitoring of the total temperature in the Hot Tunnel and should therefore permit closer control of the conditions required during experimental runs.

RECOMMENDATIONS

An investigation on the behaviour of a cooled film sensor placed in an aspirating probe, would be of interest in future. To eliminate any sensor damage or probe orifice blockage by Zirconia pebble dust, a Silicon Carbide screen would be recommended in a location upstream of the temperature section as shown in Figure 34.

The use of Tungsten Carbide (WC) material for supporting rods created a problem mainly because of WO₃ layer formation; continuous subjection to hight temperature oxidizing atmospheres, resulted in a gradual decrease in diameter, presumably through reaction of the trioxide with the carbide; this continuous decrease in diameter caused loose contact with the target which was blown off its position occasionally. Use of Silicon Carbide would be advisable.

A recently developed transistorized recording pyrometer (Ref. 6) would be of considerable value. The instrument operates on the same principle as the disappearing filament type with infrared transmitting filter $(1.4.\mu)$.

REFERENCES

- 1. Forde, J.M., Ahmed, A.M., Szpiro, E.J.,
 The McGill University High Enthalpy Supersonic Wind Tunnel
 Mechanical Engineering Research Laboratories,
 McGill University, Tech. Note 64-9, December 1964.
- 2. Lachman, J.C., Refractory Metal Thermocouples, ASME Publication 59 HT-21, Presented at the ASME-AICHE Heat Transfer Conference, Storrs, Connecticut (August 1959).
- 3. Rossler, F.,
 Temperature Measurement of Transient Phenomena,
 Temperature its Measurement and Control in Science and
 Industry, Vol. 3, Part 2, p.509.
- 4. Mathias, B.B.,
 Master's thesis, M.I.T. 1952.
- 5. Campbell, I.E.,
 High Temperature Pyrometry (1956).
- 6. Edler, S.A.,
 A Completely Transistorized Recording Pyrometer,
 Temperature its Measurement and Control in Science
 and Industry, Vol. 3, Part 2, p. 873.
- 7. The Carborundum Co.,
 Niagara Falls, N.Y. (U.S.A.)
- 8. Rhodes, T.J.,
 Industrial Instruments for Measurement and Control.
 169-172, 1941.
- 9. Armour Research Report, WADC TR-56-222, Parts I and II.
- 10. Brugel, W.,
 Strahlungsmessungen an Electrisch Geheizte SiC Staben,
 Z. Physik 127, 400 (1950).
- 11. Eckert, E.R.G. and Drake, R.M., Heat and Mass Transfer p. 365 (1959).

- 12. Buckley, H.
 On the Radiation from the Inside of a Circular
 Cylinder Part III,
 Philosophical Magazine, Vol. 17, No. 7, 576 581, (1934).
- 13. Sparrow, E.M., Albers, L.W. and Eckert, E.R.G., Thermal Radiation Characteristics of Cylindrical Enclosures, Journal of Heat Transfer, Paper No. 61 - SA - 23.
- 14. Vollmer, J.,
 Study of the Effective Thermal Emittance of Cylindrical
 Cavities,
 Journal of the American Optical Society,
 Vol. 47, 926 932 (1957).
- Breene, R.,
 J. Chemical Phys. 29, 512 (1958).
- 16. Wentick, T., Planet, W., Hammerling, P., and Kivel, B., J.Applied Phys., 29, 742 (1958).
- Tourin, R.H.,
 J. Opt. Soc. Am. <u>51</u>, 175 (1961)
- 18. Tourin, R.H.,
 Natl. Bur. Standards Circ. No. <u>523</u>, 87 (1954).
- Plyler, E.K.
 J. Research Natl. Bur. Standards 40, 113 (1948).
- 20. Plyler, E.K. and Humphreys, C.J., J. Research Natl. Bur. Standards 40, 449 (1948).
- 21. Kostowski, H.J., and Lee, R.D.,
 Temperature its Measurement and Control in Science
 and Industry, Vol. 3, Part 1, p. 453.
- 22. The General Electric Company Limited,
 Hirst Research Centre (Wembley, Middlesex, England.)
- 23. McAdams, W.H.,
 Heat Transmission (Third Edition 1954).

- 24. Port, F.J., Sc.D.,
 Thesis in Chemical Engineering, M.I.T. 1940.
- 25. Hottel, H.C. and Keller, J.D., Trans. Am. Inst. Chem. Engrs., 38, 531 - 565.
- 26. Kreith, F., Principles of Heat Transfer.
- 27. Owczarek, J.A. Fundamentals of Gas Dynamics (p. 139).
- 28. Hansen, C.F. and Heims, S.P.,
 A Review of the Thermodynamic and Transport, and
 Chemical Reaction Rate Properties of the High
 Temperature Air.
 NASA TN 4359 (July, 1958).
- 29. Wray, K.L.,
 Chemical Kinetics of High Temperature Air ARS Progress
 in Astronautics and Rocketry "Hypersonic Flow Research"
 Edited by F.R. Riddell (Academic Press N.Y. 1962) Vol. 7.
- 30. Trottier, G. and Ahmed, A.M. Cooled film Anenometer measurement in H.S. Wakes. (D.R.B. May 1966).
- 31. West, W.E., and Westwater, J.W.
 Radiation-Conduction Correction for Temperature
 Measurements in Hot Gases.
 Industrial and Engineering Chemistry J. 45, Part 2, 2152-2156.
- Dittus, F.W. and Boelter, L.M.K.,
 Univ. Calif., Pubs. Eng. <u>2</u>, 443 (1930).
- 33. Colburn, A.P., Trans. Am. Inst. Chem. Engrs., 29, 174-210 (1933).
- 34. Wilkes, G.B., Heat Insulation (pp. 165 - 193).
- 35. Valenti, A.M.,
 Report 62 7, McGill University.

- 36. Smithells, Metals Reference Book (2nd Edition, Vol. 2, p. 807).
- 37. Gubareff, G.G., Janssen, J.E. and Torborg, R.H., Thermal Radiation Properties Survey (Honeywell).
- 38. Hyde, E.P., Cady, F.E. and Forsythe, W.E., Astrophys. J., <u>42</u>, 302 (1915).
- 39. Zsombor-Murray, P.J.,
 Hypersonic Combustion Rig Orifice Design,
 Mechanical Engineering Research Laboratories Report
 No. SCS 11 (McGill University).
- 40. Leeds and Northrup (Philadelphia 44, Pa.)
- 41. Hilsenrath, J. and Klein, M.,
 Table of Thermodynamic Properties of Air in Chemical
 Equilibrium including Second Virial Corrections from
 1500°K to 15000°K.
 Arnold Engineering Development Center, Air Force Systems
 Command, AEDC TDR 63 161 (August 1963).
- 42. Hilpert, R., Forsch. Gebiete Ingenieur, 4, 215 (1933)
- 43. Stanton, T.E. and Pannell, J.R., Trans. Roy. Soc. (London), A214, 199 - 224.
- 44. Martinelli, R.C., Trans. A.S.M.E., Vol. <u>69</u>, 947 - 959, (1947).
- 45. Canadian Pittsburgh Industries Limited, 255 Decarie Boulevard, St. Laurent, P.Q., Canada.

APPENDIX I

Gas Radiation Calculation

The dependence of gas emissivity on pressure, temperature and geometry is shown in Figure 36 for water vapour. P_W is the partial pressure of the water vapour and P_T is the total gas pressure. L is the mean beam length which depends on gas geometry. Port (Ref. 24) suggests a value for L equal to 0.9 diameter when dealing with a semi-infinite cylinder of diameter D radiating to the centre of base. Test section conditions (see Fig. 37) match this configuration with the exception that the cylinder has a finite length of 1.156 inches, giving lower values for L; 0.9D will however be used, (worst condition). Figure 39 gives correction factors when dealing with pressures other than 0 and 1 atm. for P_W and P_T respectively. The partial pressure of water vapour is determined by segregating it so as to occupy the original volume but at its partial pressure and then compressing it at constant temperature to the total pressure P_T .

In this state, the compressed volume is :-

$$V_{w} = W_{w} T_{G} R / P_{w}$$

$$\dots A.1.1$$
but
$$V_{T} = W_{T} T_{G} R / P_{T}$$

$$\dots A.1.2$$

 V_{T} = total volume of air occupied originally

From A.1.1 and A.1.2

$$V_{\tau} = P_{w}/P_{T} \qquad \dots A.1.3$$

$$\frac{\sqrt{w}}{\sqrt{1}}$$
 will be assumed to be 0.02 (Ref. 35), (P. 28).

Pu = 0.02
Pr = 7 atm. (measured during experiments)

therefore Pw = 0/14 atm.

Total emissivity due to water vapour presence is

where $C_{\overline{W}}$ = correction factor determined from Figure 39.

A comparison between radiation emitted by the target and that by the gas layer will be made.

Figure 36 shows that gas emissivity increases with decrease of temperature. The worst case will be considered, i.e. minimum target temperature of 2300°R attained during the experiments

from Figure 36

from Figure 39

therefore

Total radiant energy by gas layer is

Total radiant energy by target (assumed black) is

 $T_{\rm m}$ is the average temperature of the gas layer. Martinelli's (Ref. 44) mean temperature may be used, giving

Taking the worst case, i.e. run 122 (Table 8)

$$\left(\frac{T_{M}}{T_{T}}\right)^{4} = 2.25$$

Total radiation by gas = 0.011
Total radiation by target

which may be neglected.

APPENDIX II

Error Magnitude for Gray Target

For an actual emissivity of 0.9, errors less than 1% are expected from black body assumption.

Wein's law for black body monochromatic emissive power is:-

$$E_{b,l}(T) = C_1 \lambda^{5/2} e^{\frac{C_2}{AT}}$$
 A.2.1.

The apparent black body monochromatic emissive power of this non-black body is then

$$E_{bd}(T_d) = C_1 A^{-5} / e^{\frac{C_2}{AT_0}}$$
 A.2.2.

but
$$E = \frac{E_{b,l}(T_4)}{E_{b,l}(T)}$$
 A.2.3

where

$$C_1 = 1.187 \times 10^8 \text{ BTU } \frac{4}{\text{sq. ft. hr.}}$$
 $C_2 = 2.5896 \times 10^4 \text{ °RM}$
 $C_3 = e^{\frac{C_2}{4}(\frac{1}{4} - \frac{1}{4}a)}$

substituting the various constants,

$$T = 3022^{\circ}R$$

comparing with $T_a = 3000^{\circ}R$, the error is less than 1% which may be tolerated (Assumption 9 section 1).

APPENDIX III

Glass Transmission

An optical pyrometer determines the brightness of an incandescent body at the mean effective wavelength (Section 3.1) between brightness and colour temperatures of the body; consequently the presence of any glass window between target and instrument will cause an apparent temperature measurement essentially lower than the true temperature due to glass absorption characteristic, such a characteristic is shown in Figure 38 for the pyrex glass used. The brightness and colour temperatures are those of a black body having the same brightness and colour respectively; hence the existing black body conditions establish identical values for the brightness and the colour temperature both being equal to the true body temperature. Glass absorption effect is seen from the following:-

The maximum temperature attained by the pyrex glass (gray) was below 1000°C for the entire set of runs. At such temperatures no monochromatic radiation is expected to influence the pyrometer's readings; this is noticed from the spectral distribution of monochromatic emissive power for black bodies (Ref. 26) which have essentially higher values than gray bodies.

APPENDIX IV

When theory is the basis for air temperature determination, accurate knowledge and control of the pebble bed temperature is very important as on it depends the final air temperature (Ref. 35). The existing hot tunnel conditions allow only an approximate value for the pebble bed temperature to be obtained.

The amount of heat lost to the atmosphere through the Tunnel wall, as air travels from the furnace to the temperature section (Fig. 2), is based mainly on reasonable assumption drawn from operation experience. Finally the assumption that air leaves the furnace with the same temperature as the pebbles also introduces some inaccuracy. It was found during the experiments (Section 4.2) that the air temperature was always lower than that of the pebbles; depending on the mass flow rate this variation was as much as 150°K in some cases.

The combined effect of these assumptions does result in some inaccuracy.

APPENDIX V

A) Air Properties

Use of air properties at bulk (Ref. 32) or Film (Ref. 33) temperature, is the classical approach when determining true air temperatures from thermocouple or optical pyrometer readings.

Martinelli (Ref. 44) suggests

$$\frac{T_m - T_w}{T_c - T_w} = 0.85 \qquad \dots A.5.1.$$

for the range of Prandtl numbers (0.7 - 0.8) and Reynolds numbers (12000 - 30000) considered.

B) Mass Flow Rate

Reference 39 gives the method of determining air mass flow rate using a square edge orifice.

C) Velocity

Failure of the Pitot tube due to high temperature pebble dust ejection, necessitated using an average velocity based on the mass flow rate and test section area. For the range of Reynolds Numbers, (turbulent flow) investigated, the ratio of average velocity to maximum velocity $\frac{U_{av}}{U_{max}}$ is given by Stanton (Ref. 43) to vary between O.8 and O.85. These values may be used for regions inside the turbulent core without appreciable error.

D) Reynolds Number based on Section Diameter D

The turbulent nature of the flow field is clear from the range of Reynolds numbers obtained 12000 - 30000.

E) Heat Transfer Coefficient by Forced Convection (hc)

Hilpert's (Ref. 42) equation is used to calculate the Nusselt number based on probe diameter (d) for thermocouple corrections or on supporting rod diameter (d) for Optical pyrometer corrections.

$$Nu_d = 0.43 + c (Re_d)^m :.... A.5.2$$

Values of c and m are given in Reference 42 or 11.

F) Heat Transfer Coefficient by Radiation (hr)

The radiant heat transfer term g_{Q_R} in equation 2.6 (Section 2.4), may be expressed in the following conventional form for an element g_{X} of the probe (Figure 19b).

where Jow is the gray body shape factor which allows for departure of the surface from black body conditions.

$$\frac{1}{1-w} = \frac{1}{\frac{f_1}{E_1} + \frac{1}{F_1-w} + \frac{A_1 f_2}{A_w E_w}} \dots A.5.4$$

F = Configuration factor = 1 for the existing temperature section, subscripts 1 and w refer to thermocouple probe (or target supporting rod) and wall conditions respectively.

The term $A_1 \rho_w/A_w E_w$ in equation (A.5.4) is 0.0055 for thermocouple and 0.0272 for supporting rod and may be neglected in comparison to $(\frac{\rho_1}{E_1} \ + \ \frac{1}{F_{1-w}} \)$

therefore

$$F_{1-w} = \frac{1}{\frac{\rho_1}{E_1} + 1} = E_1$$

Fourrier's suggested alternate form may be written

$$Q_R = hr (T - Tw)P Sx$$
 A.5.5

equate A.5.3 and A.5.4

$$hr = \frac{6J_{1-w}(T^{4}-T_{w}^{4})}{(T-T_{w})} \dots A.5.6$$

The authors of Reference 31 assume hr constant and equal to the value at thermocouple tip (T_E) or radiation target (T_T) whichever the case may be. Therefore,

a.
$$hr = G - \frac{1}{1-w} \left(\frac{1}{1-w} - \frac{1}{1-w} \right)$$
 A.5.7

for thermocouple reading correction

b.
$$hr = \sigma J_{1-w} \left(T_{T}^{4} - T_{w}^{4} \right) \dots A.5.8$$

for Optical Pyrometer reading correction

G) Alumina (Thermocouple Insulator)

The total emissivity of Alumina is given in Table 6 as suggested by two different references. The figure 0.35 was used.

Thermal conductivity of Alumina is 6 BTU hr⁻¹ ft⁻² in^o_F⁻¹

(Ref. 34) for temperatures above 1200°F while that of Platinum is

480 BTU hr⁻¹ ft⁻² in^o_F⁻¹ (Refs. 23 and 34). The equivalent conductivity of this parallel connected heat flow path is then

$$\frac{K_{1}q_{1} + K_{2}q_{2}}{q_{1} + q_{2}}$$
 A.5.9

subscripts 1 and 2 refer to Alumina and Platinum respectively. The overall probe diameter was 0.2 inches while the thermocouple wires were 24 ga. each.

(Note: The effect of air gap conductivity, between the thermocouple wires and insulator, is neglected as it is less than 1% in comparison to the effects of Alumina and Platinum.)

H) Zirconia (surrounding enclosure)

Table 7 gives the total emissivity as taken from four different references.

Tungsten Carbide (Radiation target supporting rods)

Reference 36 suggests a value of .19 cal. cm⁻¹ sec⁻¹ °C⁻¹

for thermal conductivity while the total emissivity is taken as 0.85 allowing effects of tungsten trioxide formation around the rod.

APPENDIX VI

The corrections applied to the instrument readings of Table 8 will be considered in detail for run number 321.

- a) Corrections applied to radiation target temperature
- i) Wall and target temperatures (T $_{\!W}$ and T $_{\!T}$) :-

The readings of the optical pyrometer for wall and target are 1872°F (1294°K) and 2147°F (1448°K) respectively. Glass absorption effect is determined from Eq. A.3.1 (Appendix III).

$$\mathcal{L}_{A} = 0.9 \quad \text{(Fig. 38)}$$

using Planck's law for $E_{b,\lambda}$ and an effective wavelength of 0.6633 μ , the true wall and target temperatures are 1887°F and 2166°F respectively.

ii) Support rod properties :-

Cross-sectional area (a) = 0.000341 sq. ft. (diameter was reduced to 1/4 inch)

Perimeter = 0.0431279 ft.

Thermal Conductivity = 45.97 BTU hr. $^{-1}$ ft. $^{-1}$ oF $^{-1}$ (Ref. 36) Length (L) = $\frac{1.031}{12}$ ft. (Fig. 19b)

iii) Heat transfer coefficient by forced convection (hc) :-

Equation A.5.2 (Appendix V) is used to determine hc. The air properties are taken at a mean temperature as suggested by Martinelli (Ref. 44)

hc is therefore 63.2 BTU hr. -1 ft. -20 F -1

- iv) Heat transfer coefficient by radiation (\overline{hr})

 Equation A.5.8 (appendix V) gives $\overline{hr} = 89.8$ BTU $hr.^{-1}$ ft. $^{-2o}$ F $^{-1}$ Substituting these values in Equation 2.9 (p. 14), the true air temperature (T_G) is therefore 2757 o F (1787 o K).
- b) Corrections applied to thermocouple readings at location 5 (Fig. 21)
- i) Wall temperature :Same procedure as in (a).
- Thermocouple properties:
 Thermocouple tip temperature is $2381^{\circ}F$ (1578°K).

 Cross-sectional area = $\frac{11}{4}$ ($\frac{0.2}{12}$) sq. ft.

 Perimeter = $\frac{1}{4}$ ($\frac{0.2}{12}$) ft.

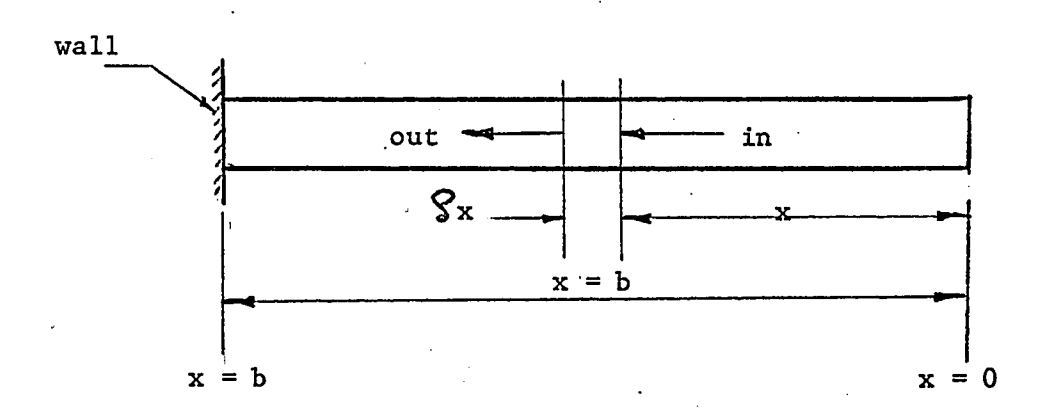
From Eq. A.5.9 (Appendix V) the thermal conductivity is 1.2979 BTU hr. $^{-1}$ ft $^{-10}$ F $^{-1}$, Length b = $\frac{1.05}{12}$ ft. (Fig. 21)

- iii) Heat transfer coefficient by forced convection (hc):
 The same procedure as in (a). hc = 48.86 BTU $hr.^{-1}ft.^{-20}F^{-1}$
- iv) Heat transfer coefficient by radiation (hr) Eq. A.5.7 (Appendix V) gives hr = 42.26 BTU hr. $^{-1}$ ft. $^{-20}$ F $^{-1}$. Substituting these values in Eq. 2.8 (p. 14) the true air temperature (T_G) at location 5 is therefore determined to be 2653° F (1748° K).

In the same manner, the true air temperatures are determined at locations 1, 2, 3 and 4 by using the appropriate values for b from Fig. 21.

Table 9 shows these results.

Appendix VII



Equation 2.5 (p. 13) is derived as follows:-

For twe x and twe $\frac{dT}{dx}$,

Heat entering element $\Im x$ by conduction :- -Ka $\frac{dT}{dx}$

Heat leaving element $g_{\mathbf{x}_{i}}$ by conduction :-

$$= - Ka \frac{dT}{dx} + \frac{d}{dx} (- Ka \frac{dT}{dx})$$

Net heat leaving element :

- Ka
$$\frac{dT}{dx}$$
 + $\frac{d}{dx}$ (- Ka $\frac{dT}{dx}$) \times - (- Ka $\frac{dT}{dx}$)

$$= - Ka \frac{d^2T}{dx^2} S_x$$

TABLE 1

Material Applicability to High Temperatures

Refractory Materials	Advantages	Disadvantages	Effects	Use
1. Metals		 Low physical strength Lack of resistance to oxidation at high temperatures 	1) Oxidation2) Material deterioration	Unsatisfactory
2. Refractory Oxides	Very stable in oxidising atmospheres	 Low thermal conductivity Low mechanical strength Moderate melting point 	 Material softening Thermal shock 	Fair
3. Silicides	Excellent resistance to oxidation	1) Moderate melting point2) Brittle	Softening	Fair
4. Sulfides		 Relatively low melting point Susceptible to oxidation at elevated temperatures 	1) Softening2) Material deterioration	Unsaitsfactory
5. Borides	High melting points	Little resistance to oxidation	1) Oxidation2) Material deterioration	Unsatisfactory
6. Cermets	High melting points			Satisfactory
7. Graphite	 High mechanical strength Good resistance to thermal shocks 	Little resistance to oxidation at high temperatures	Material deterioration	Unsatisfactory
8. Carbides	 High melting points Fair resistance to 			Satisfactory

oxidation

1.7

TABLE 2.

Order of Material Preference in Use for Radiation Targets

Material	Experimented	Not Experimented
Silicon Carbide Foam	1 (ref. 7)	
Cellulose Carbon		2 (ref. 22)
Sintered Boride	3 (ref. 7)	
Carbide base Cermets		4

TABLE 3

Apparent Emissivities $(E_a(r))$ With Cavity (Ref. 13)

Т. ,	E = 0.9	E = 0.75	E = 0.5
L/d		•	
4	0.9984 - 0.9986	0.9956 - 9961	0.9880 - 0.9887
3			0.9768 - 0.9793
2 .	0.9936 - 0.9945	0.9815 - 0.9842	0.9460 - 0.9540
1	0.9785 - 0.9848	0.9389 - 0.9553	0.8394 - 0.8776
0.5	0.9482 - 0.9708	0.8626 - 0.9180	0.6878 - 0.7914
0.25	0.9191 - 0.9602	0.7937 - 0.8901	0.5693 - 0.7317

T. A B L E 4 (a)

Changes due to variation in temperature interval, in the mean effective wavelength of red glass. (Ref. 38)

Temp. Interval (^O K)	Mean Effective Wavelength for Red Glass No. F-4512
	•
1336 - 1600	0.6649
1336 - 1822	0.6646
1336 - 3100	0.6634
1600 - 1822	0.6641
1822 - 2400	0.6629
1822 - 3100	0.6624
2400 - 3100	0.6617

T A B L E 4 (b)

Effective wavelength as different temperatures are approached (Ref. 38)

Temperature (^O K)	Effective Wavelength (µ)
1300	0.6655—
1500	0.6648
1700	0.6641
1900	0.6635 Mean =
2300	0.6633 µ
2700	0.6616

T A B · L E 5

Range of Investigation

Pressure (atm.)	Mass Flow Ra	te (1bs/sec.)	Total Temperature (^O K)		
Max.	Min.	Max.	Min.	Max.	
7 - 8	0.10	0.20 or chocked flow rate whichever lower	1000	2200	
Tunnel design pressure allowable	Below this value the time required to reach steady state was excessive.	Ejection of Zirconia pebble segments, was excessive above this value.	Specified limit for Optical Pyrometer	Higher values may be attained by increasing H ₂ mass flow through afterburner	

۱ 51

TABLE 6 Total Emissivity of Alumina (Thermocouple Insulator)

Temp. F	WILKES (34)	Campbell (5)	Mean value
1200	0.37		0.37
1600	0.31	• .	0.31
1832	•	0.28	0.28
2012		0.27	0.27
2192		0.28	0.28
2372		0.30	0.30
2400	0.34	0.31	- 0.325
2552		0∶34	0.34
2700	0.37	0.36	0.365
2732		0.365	0.365

TABLE 7 Total Emissivity of Zirconia (Section Wall)

Temp. F	WILKES (34)	Ref. (37)	Ref. (9)	Campbell (5)	Average Value
1200	0.44	0.56	0.46	0.46	.48
1400		0.53	0.41	0.37	0.437
1600	0.33	0.53	0.39	0.34	. 0.39
1800		0.47	0.37	0.315	0.385
2000	0.31	0.45	, 0.36	0.305	0.356
2200	·	!	0.37	0.30	0.335
2400	0.25		0.37	0.26	0.293
25 50	0.22		0.38	0.21	0.27

T A B L E 8

	~, ~~~		~~~~~					~ `			
Run No.	Mass Flow	Test Section Pressure		Trave	ersing The	rmocouple			Optical (°K	Pebble Bed Temperature	
	lbs/sec	p.s.i.a.	Loc. 1	Loc. 2	Loc. 3	Loc. 4	Loc. 5	Wall	Target		(°K)
											THE PROPERTY OF THE PROPERTY O
111	0.1050	51	1089	1201	1215	1224	1245	1022	1125	1362	
121	0.1095	56	1289	1361	1400	1429	1437	1141	1282	1636	·
221	0.1480	85	1479	1499	1532	1554	1578	1255	1418	1803	
2 11	0.1495	82	1267	1323	1331	1344	1353	1186	1266	1448	1490 - 1550
311	0.1850	102	1310	1339	1349	1356	1365	1200	1288	1469	
321	0.1850	110	1487	1532	1552	1576	1578	1294	1448	1787] .
. 122	0.1060	56	1350	1430	1455	1479	• 1500	1193	1335	1706	
212	0.1510	85	1225	1274	1287	1302	1310	1168	1233	1379	1400 - 1450
222	0.1620	90	1462	1503	1524	1545	1566	1259	1413	1761	
113	0.1335	71.5	1179	1255	1272	1277	1295	1115	1199	1388	
213	0.1730	72	1289	1330	1341	1350	1375	1183	1275	1461	1475 - 1525
223	0.1680	84	1437	1487	1504	1510	1520	1250	1380	1669	
114.	0.1050	47	1290	1351	1375	1390	1406	1137	1260	1568	
124	0.1050	52.5	1499	1557	1583	1600	1625	1376	1493	1863	1595 - 1645
224	0.1350	75	1595	1661	1687	1700	1725	1478	1592	1950	
115	0.0985	42	1258	1361	1382	1395 .	1411	1198	1300	1582	1610 - 1660
116	0.1130	85	Air Te	mperature	too high fo	or Thermor	ounle	1177	1326	1747	1780 - 1850
126	0.1130	· 92		······································			Jupic	1481	1645	21.97	

Table 9: Instrument Readings and Corrected Air Temperatures for Run Number 321

		Travers	Optical Pyrometer (^O K)				
	Loc. 1 Loc. 2 Loc. 3 Loc. 4 Loc. 5				Wall	Target	
Instrument Readings	1487	1532	1552	1576	1578	1294	1448
Corrected Air Temperatures	1590	1666	1701	1744	1748		1787

- 55 -

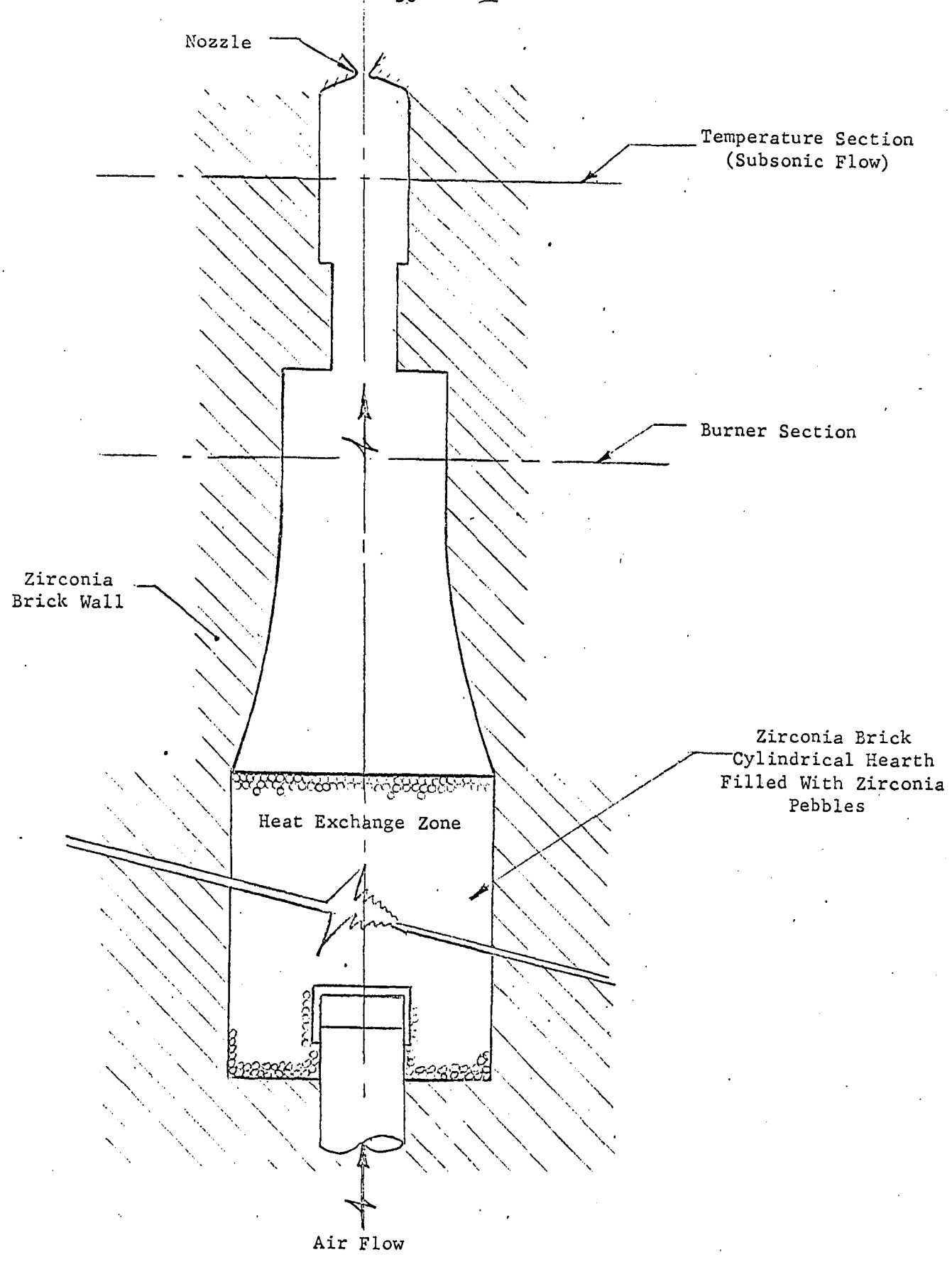


FIGURE 2 - Temperature Section Location
Relative to Pebble Bed and Nozzle

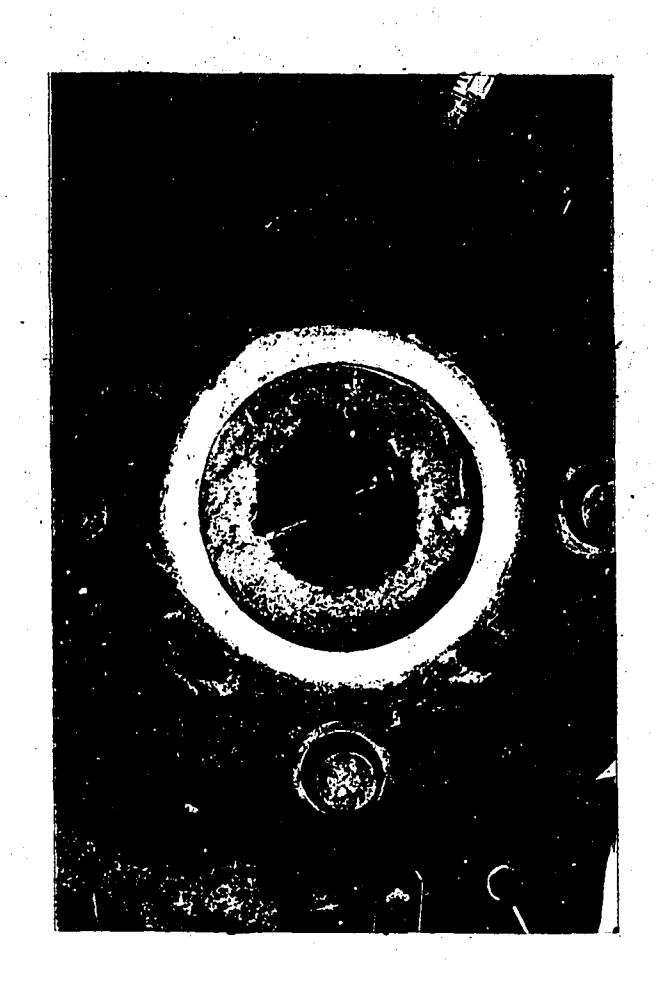


FIGURE 3

Radiation Target With Supporting Rods

This view shows the plan view of the temperature section

 \bigcirc

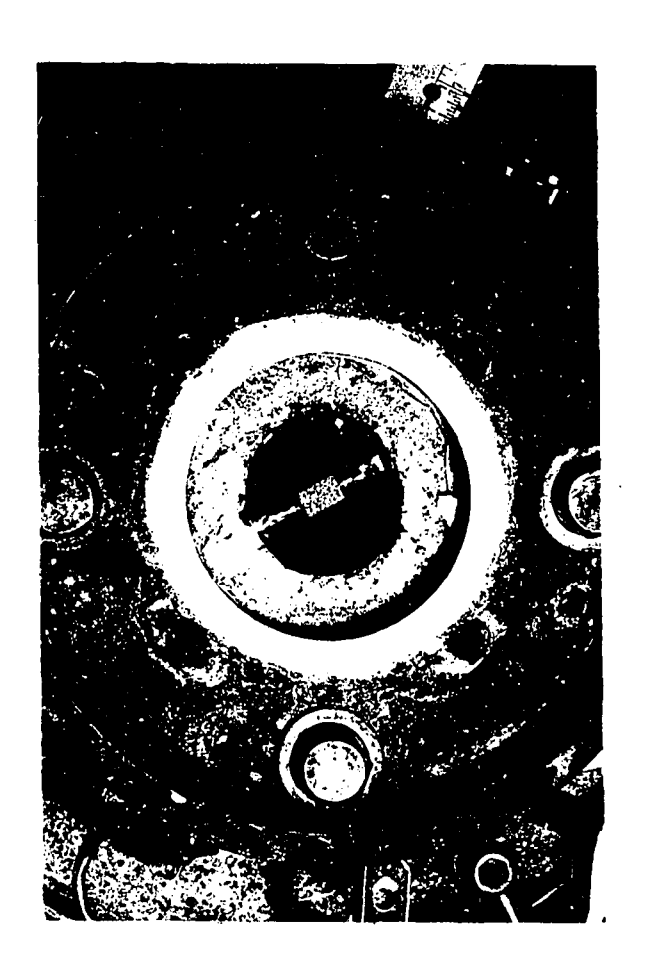
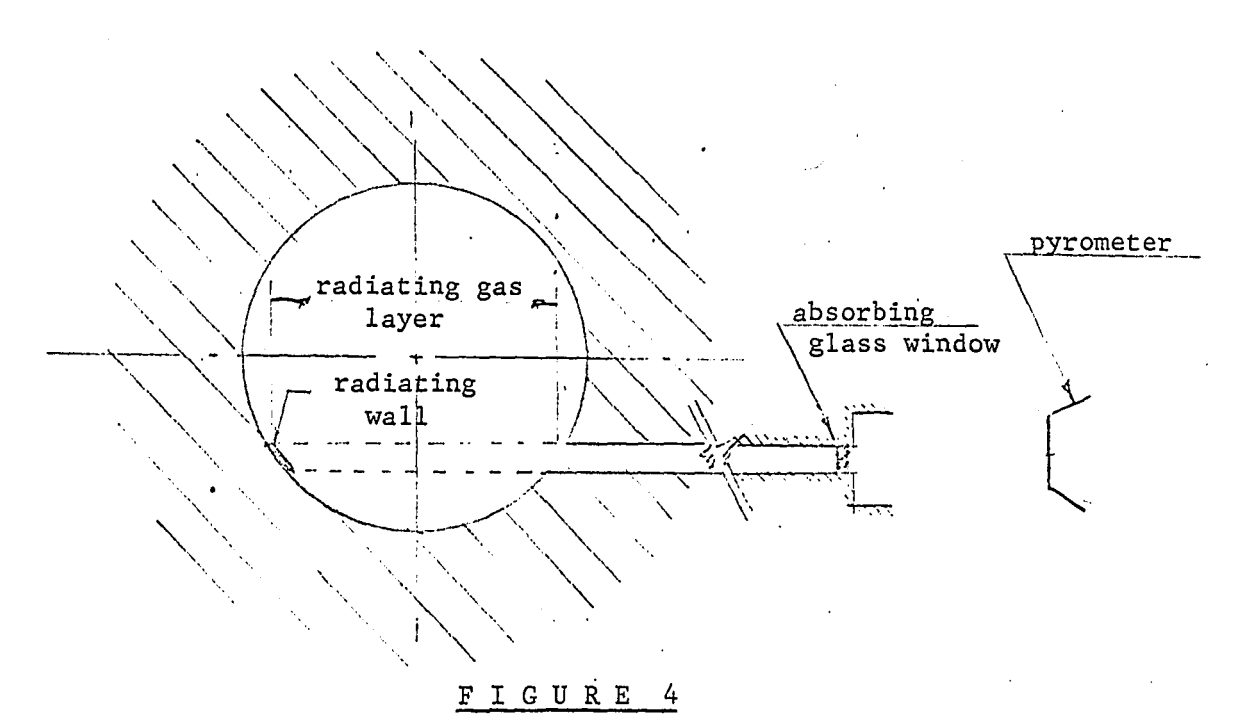


FIGURE 3

Radiation Target With Supporting Rods

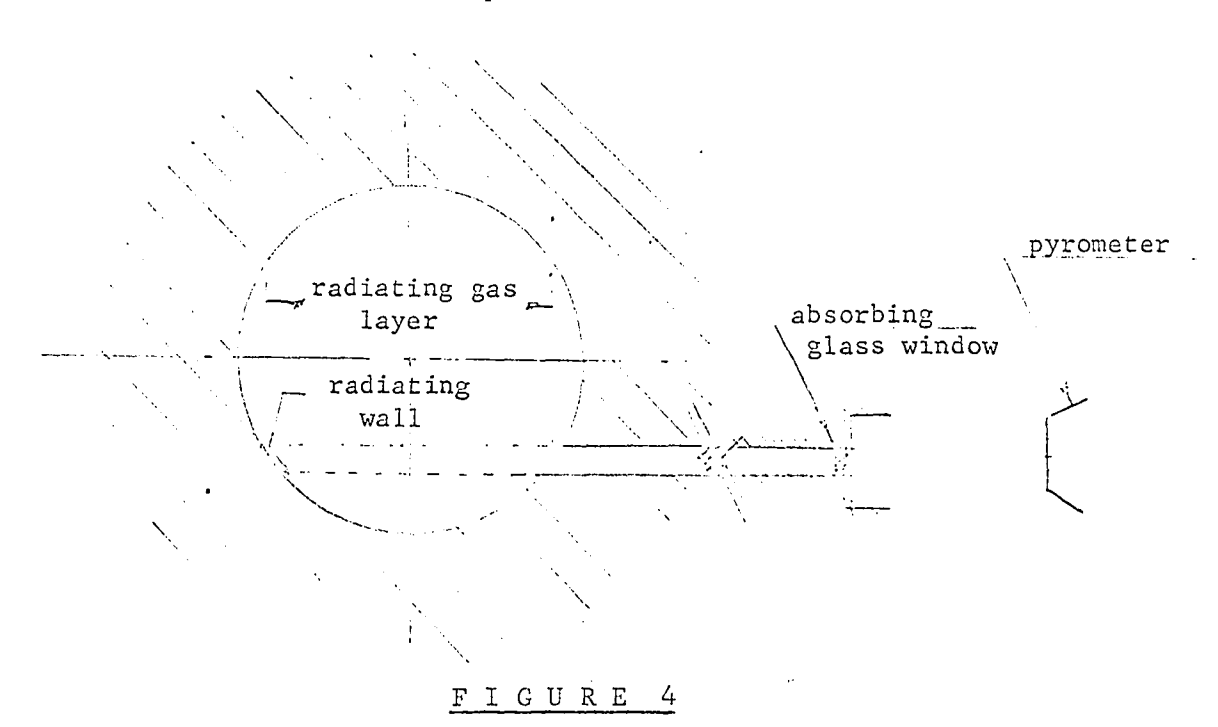
This view shows the plan view of the temperature section





Radiating and Absorbing Mediums Between Pyrometer and Radiating Wall



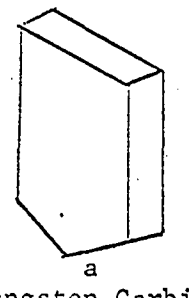


Radiating and Absorbing Mediums Between Pyrometer and Radiating Wall

RADIATION TARGET

PROCESS
During Experiment

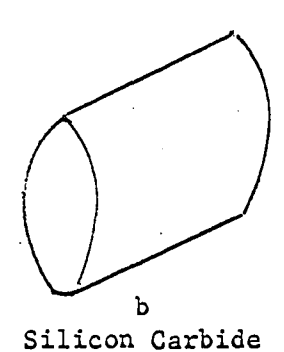
CONSEQUENCE



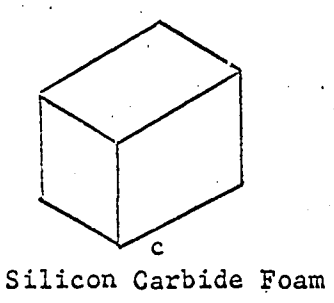
1. Rapid Oxidation

Serious Material Deterioration

Tungsten Carbide



- 1. Slight Oxidation
- 2. Steep temp. gradient
- 1. Thermal Shock
- 2. Mechanical Failure



Negligible Oxidation

None

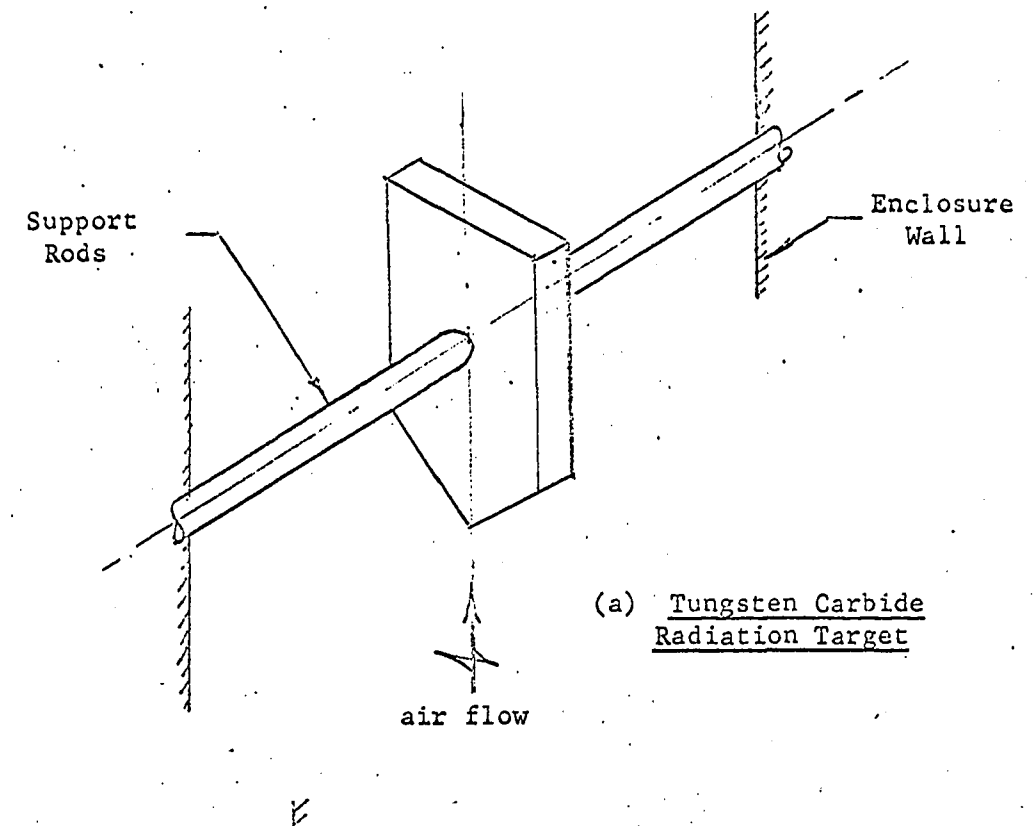
Sintered Boride No. 6
Same configuration as
in C.

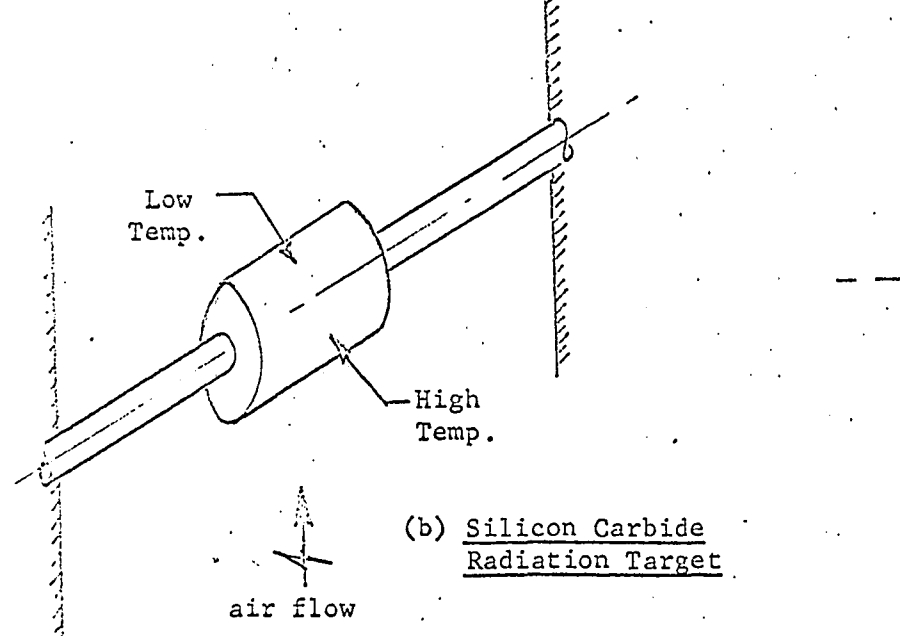
Tolerable Oxidation

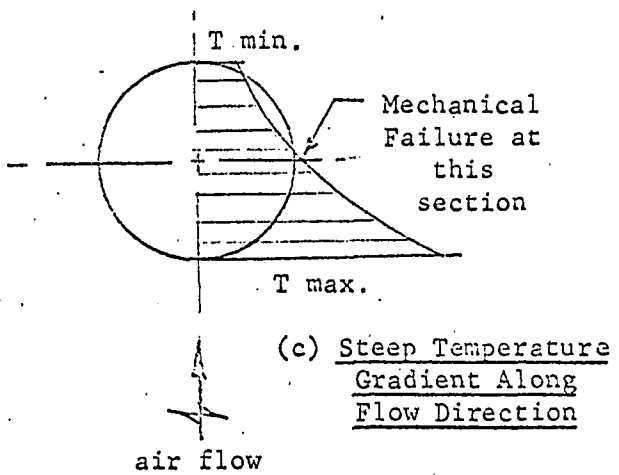
Tolerable Material Deterioration

FIGURE 5

Effects of High Temperature Oxidizing Atmospheres on Various Target Materials







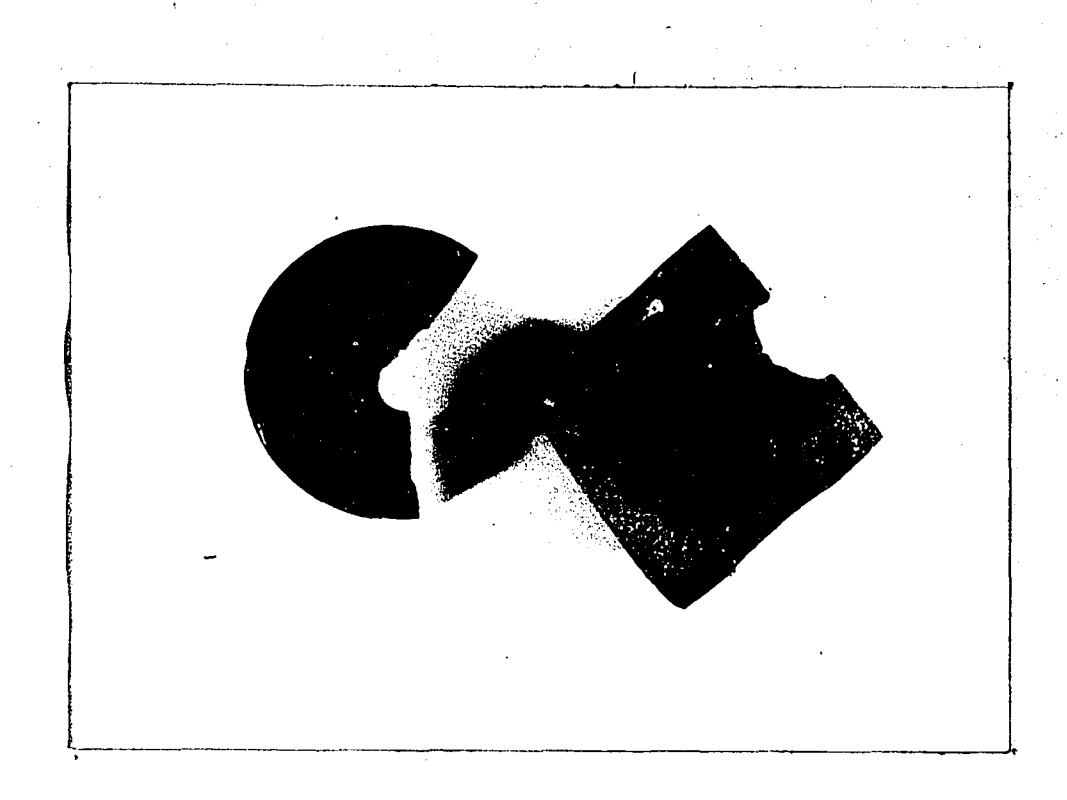


FIGURE 7 - Silicon Carbide Target Failure by Thermal Shock

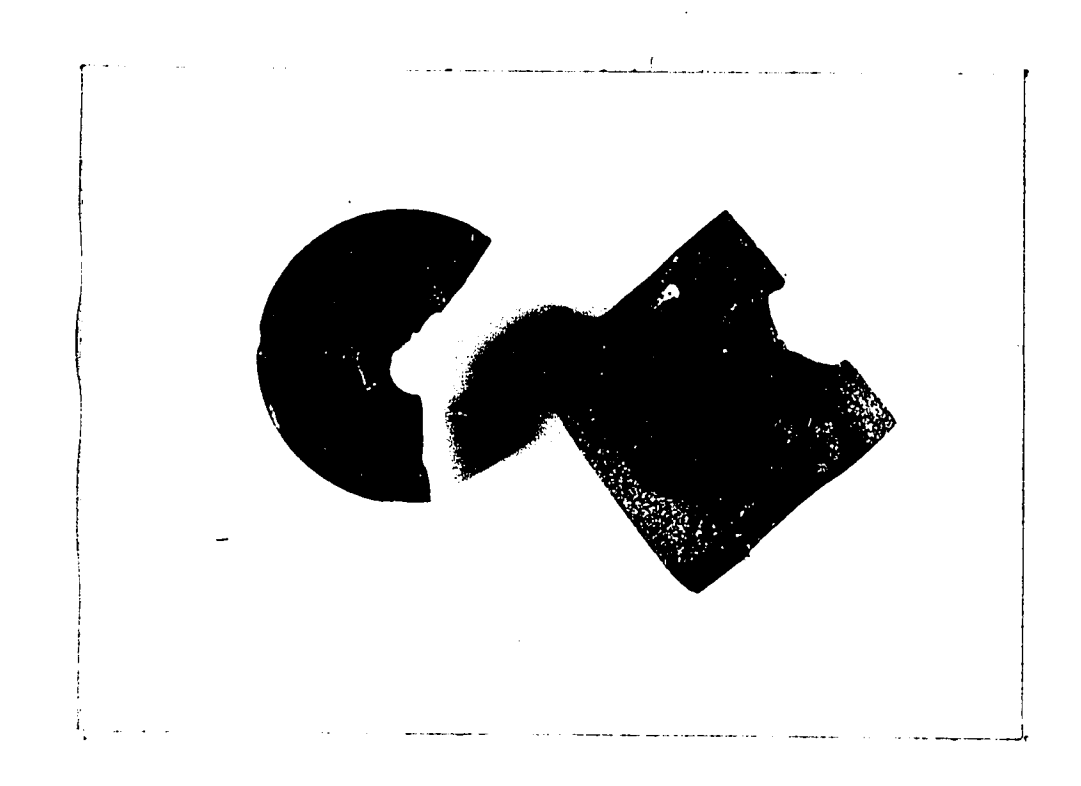


FIGURE 7 - Silicon Carbide Target Failure by Thermal Shock

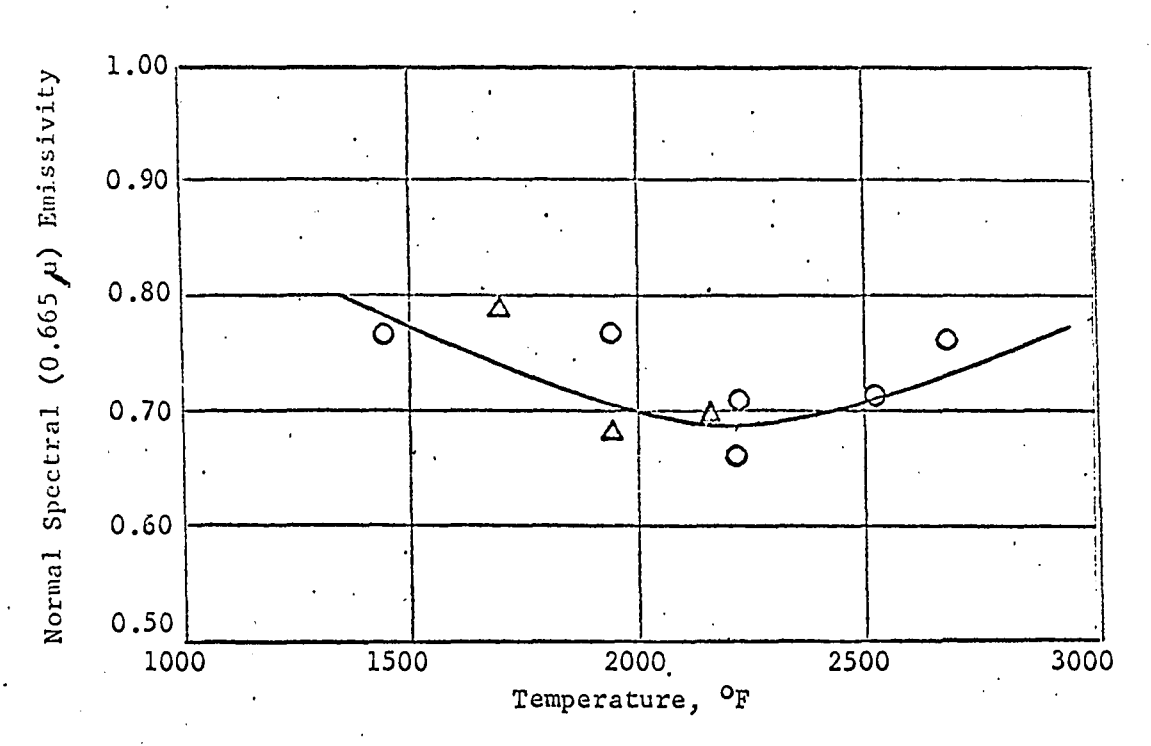


FIGURE 8 - Normal Spectral (0.665 μ)

Emissivity of Silicon Carbide - Ref. 9

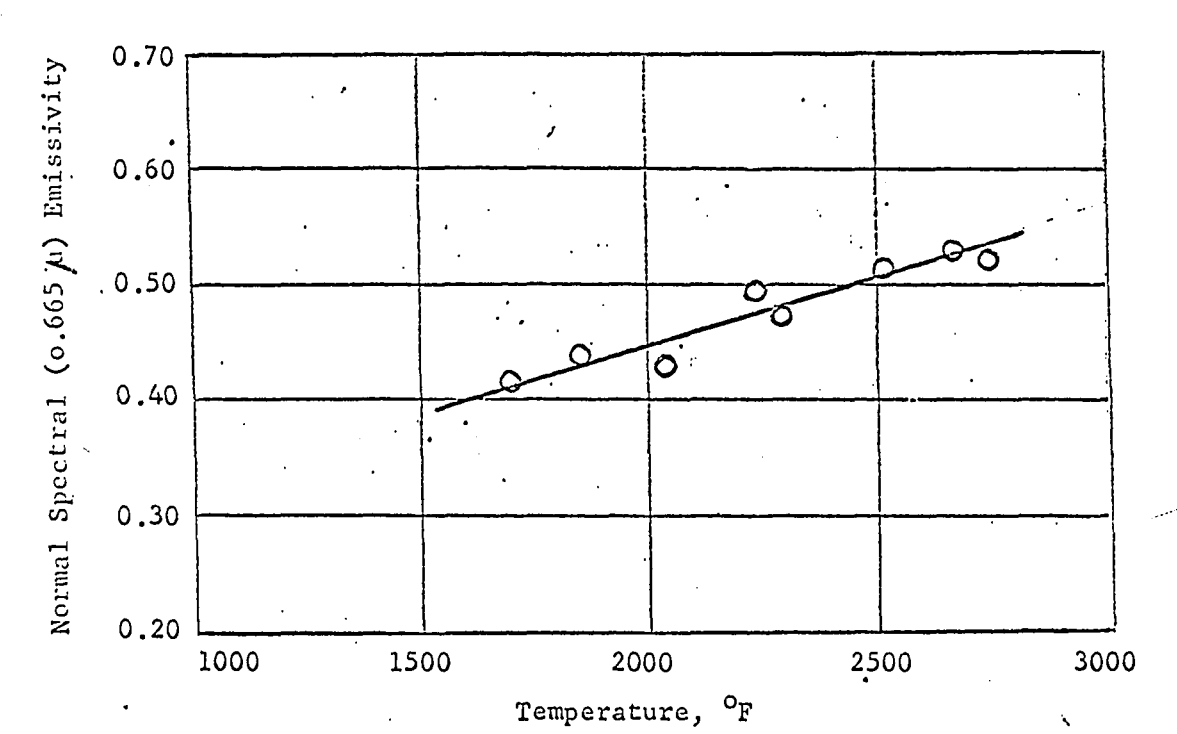
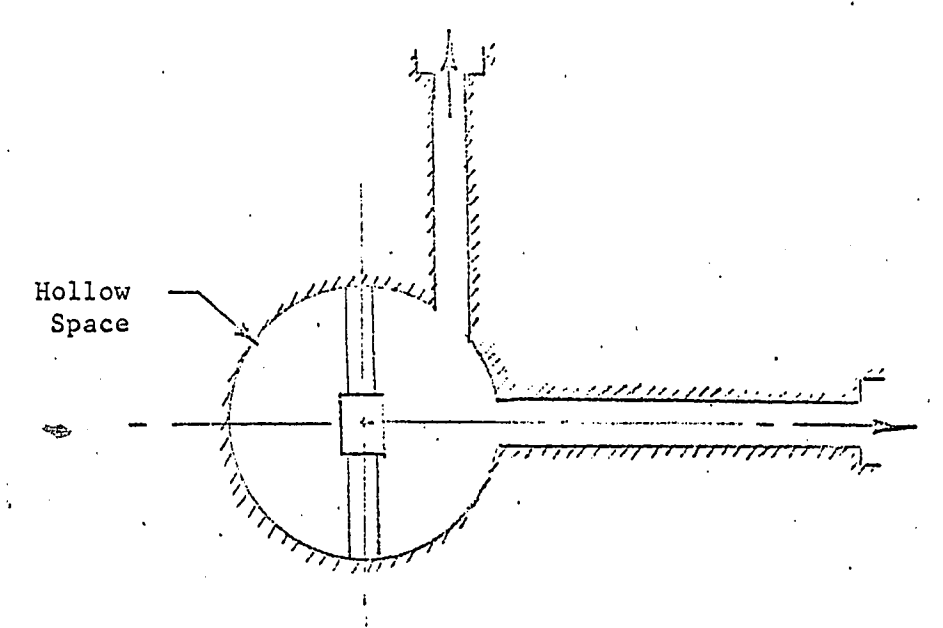


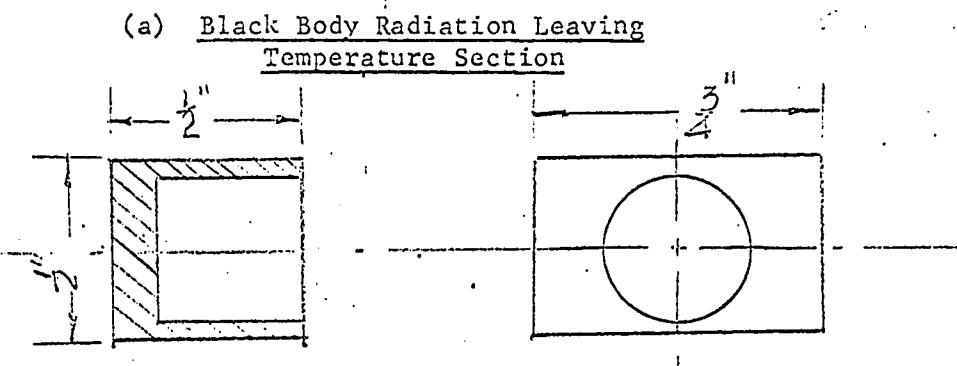
FIGURE 9 - Normal Spectral (0.665 µ)

Emissivity of Zirconium Oxide

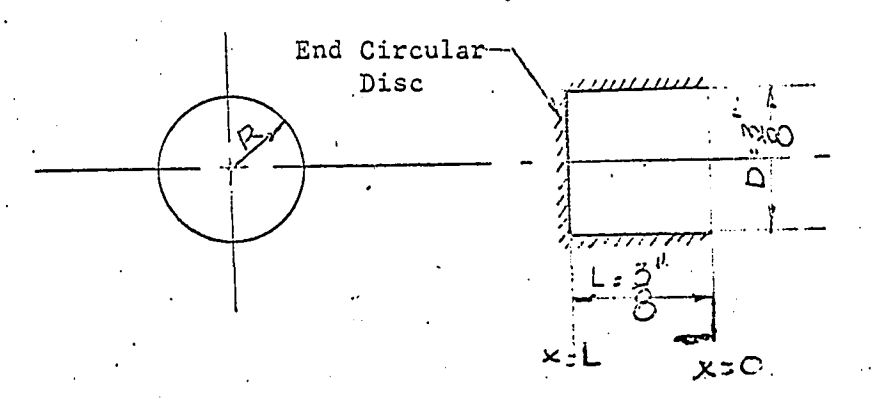
Calcium Stabilized

(Ref. 9)





Cylindrical Cavity in Target



(c) Cavity

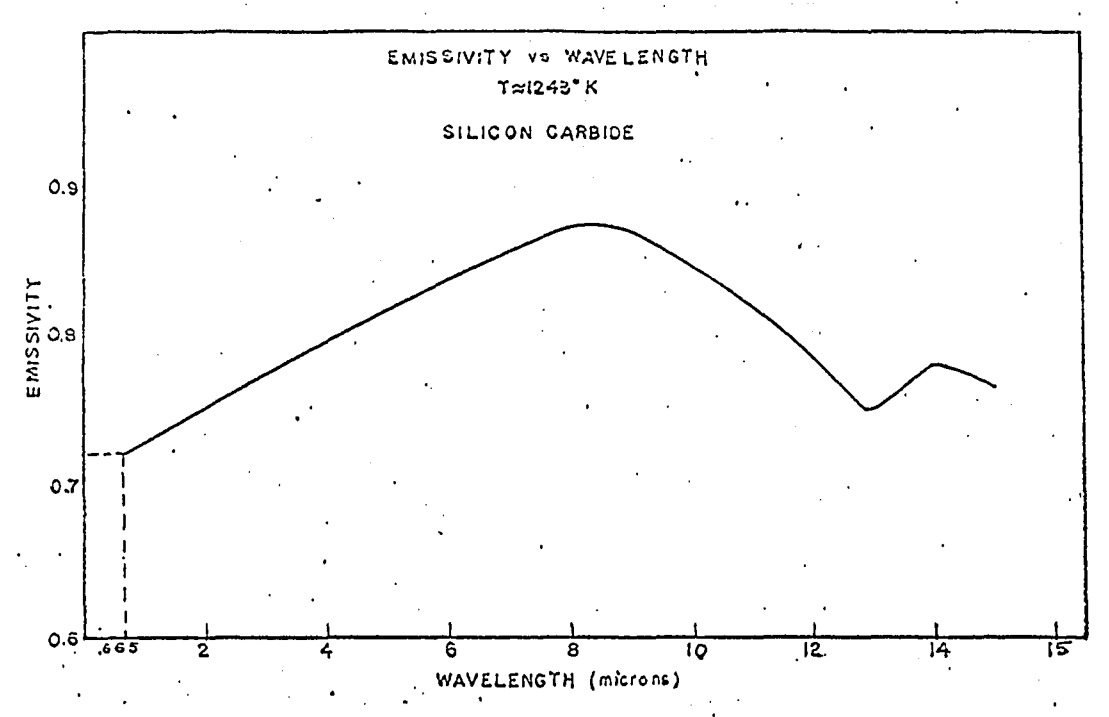


FIGURE 11 - Ref. 10

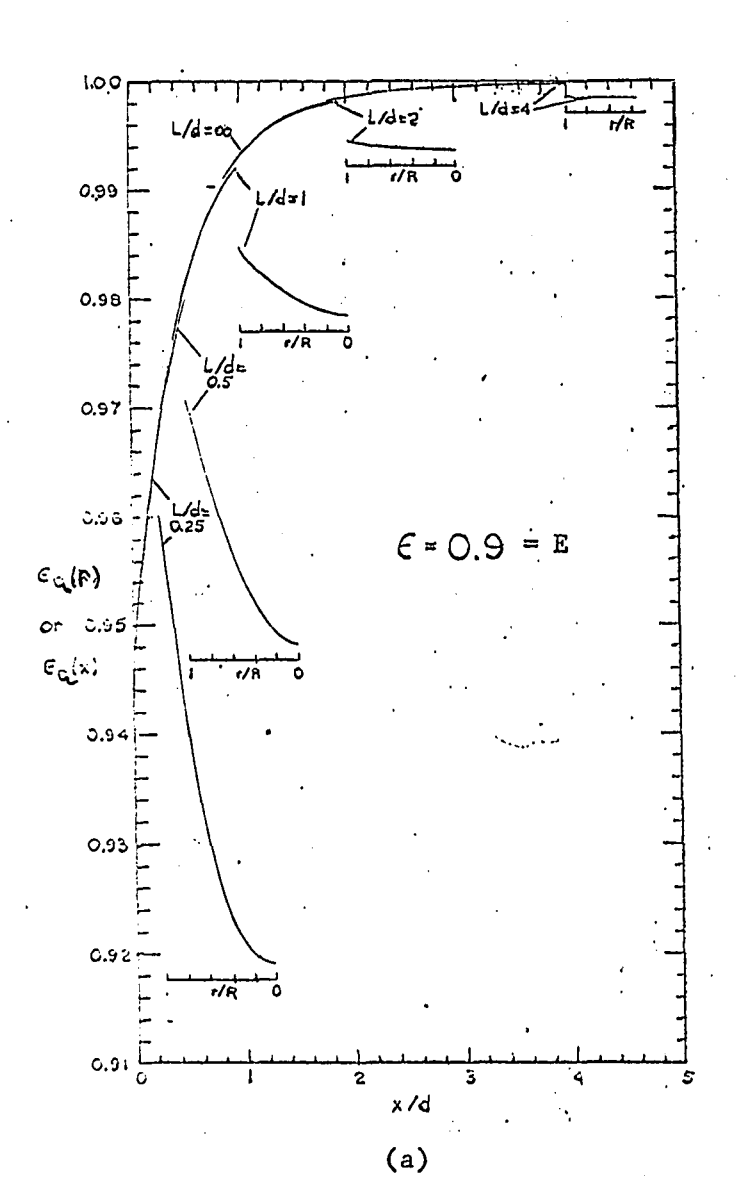


FIGURE 12 - Apparent (effective) (E_a(t))
emissivity with Cavity

(Ref. 12)

Symbols for fig. 12 (a,b, and c) :-

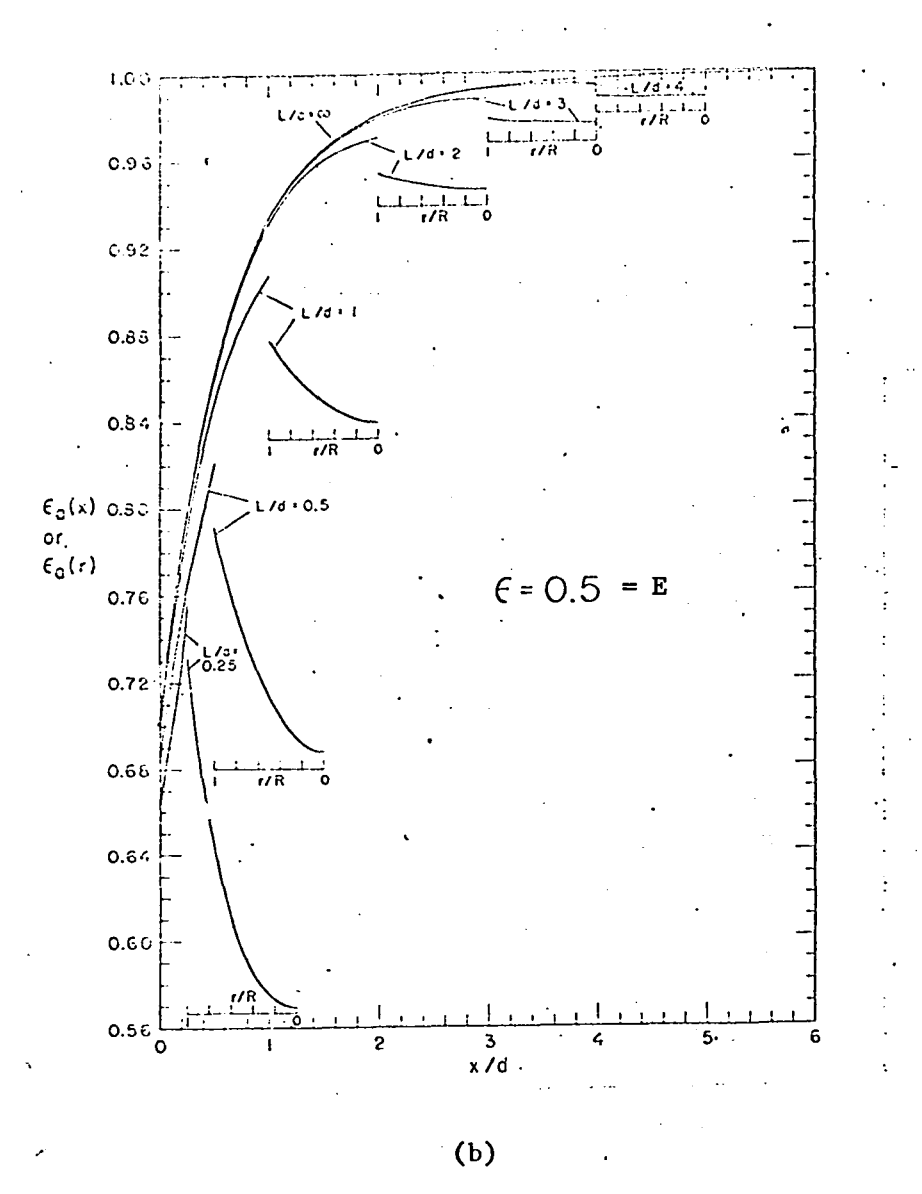
 ϵ = E = emissivity

 $\mathcal{E}_{a}(\mathbf{r}) = \mathbf{E}_{a}(\mathbf{r}) = \text{effective emissivity}$

along radius of circular end disc of cavity.

x = distance from mouth of cavity

d = diameter of cavity.



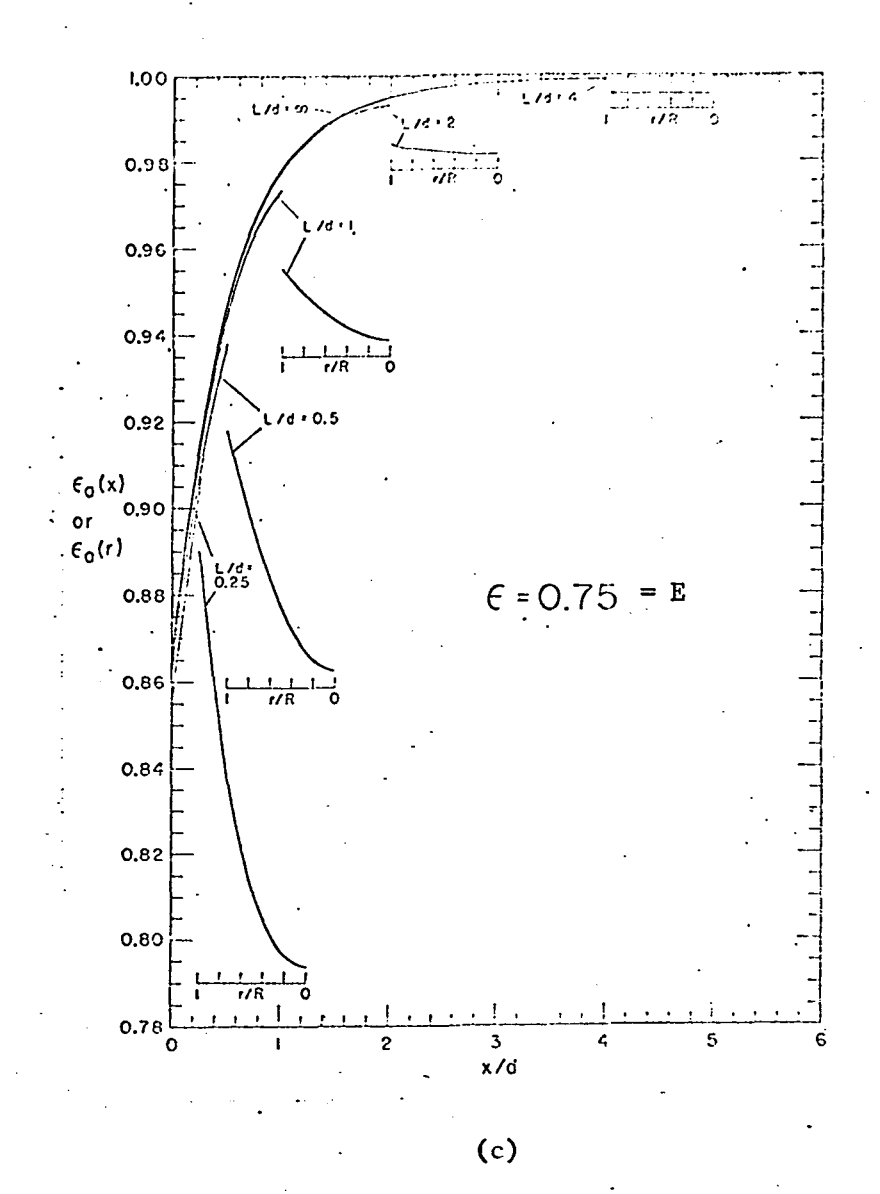


FIGURE 12 - Apparent (effective) emissivity (E_a(r))
with Cavity (Ref. 12)

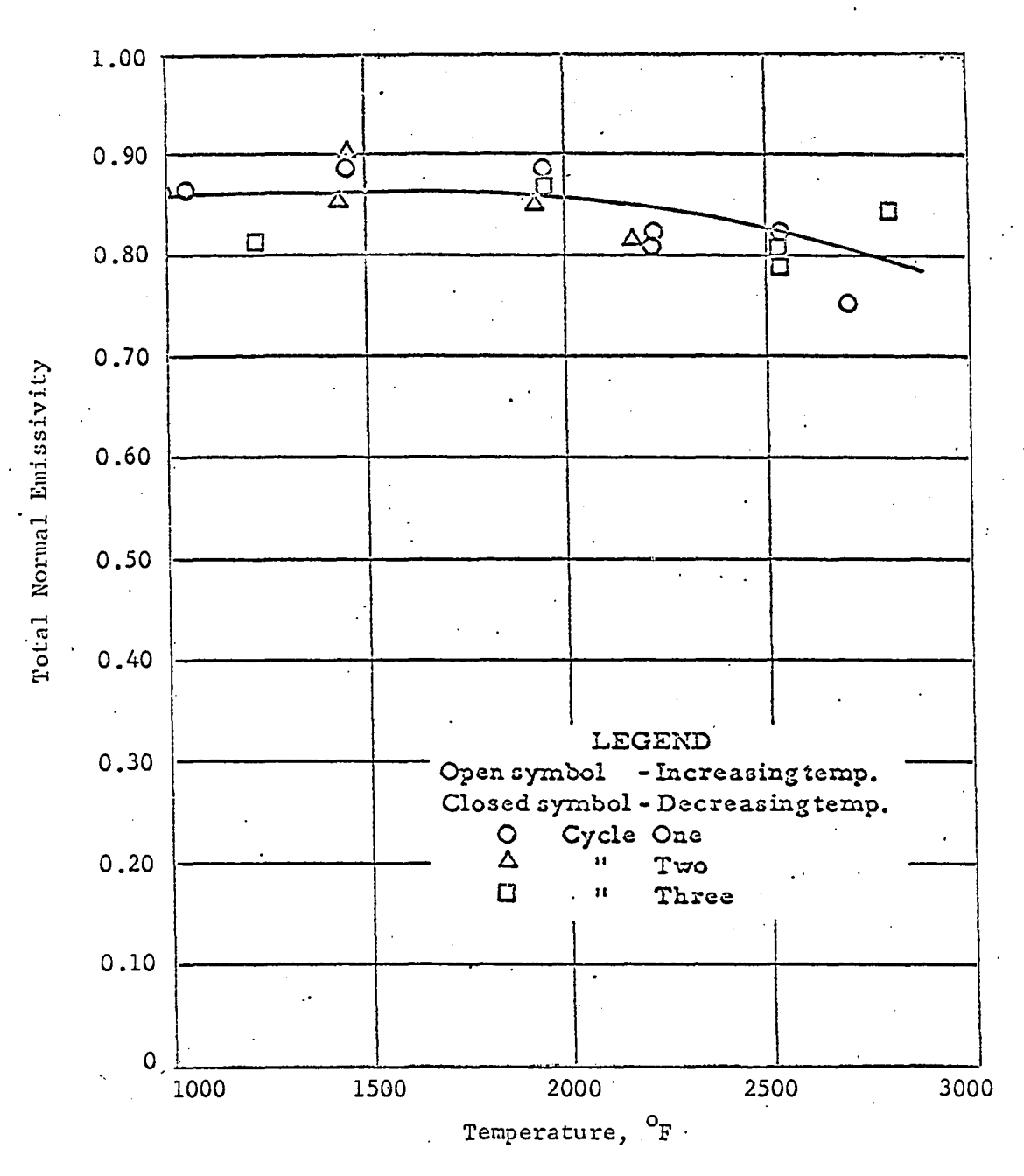


FIGURE 13 - Total Normal Emissivity in

Air of Silicon Carbide (Ref. 9)

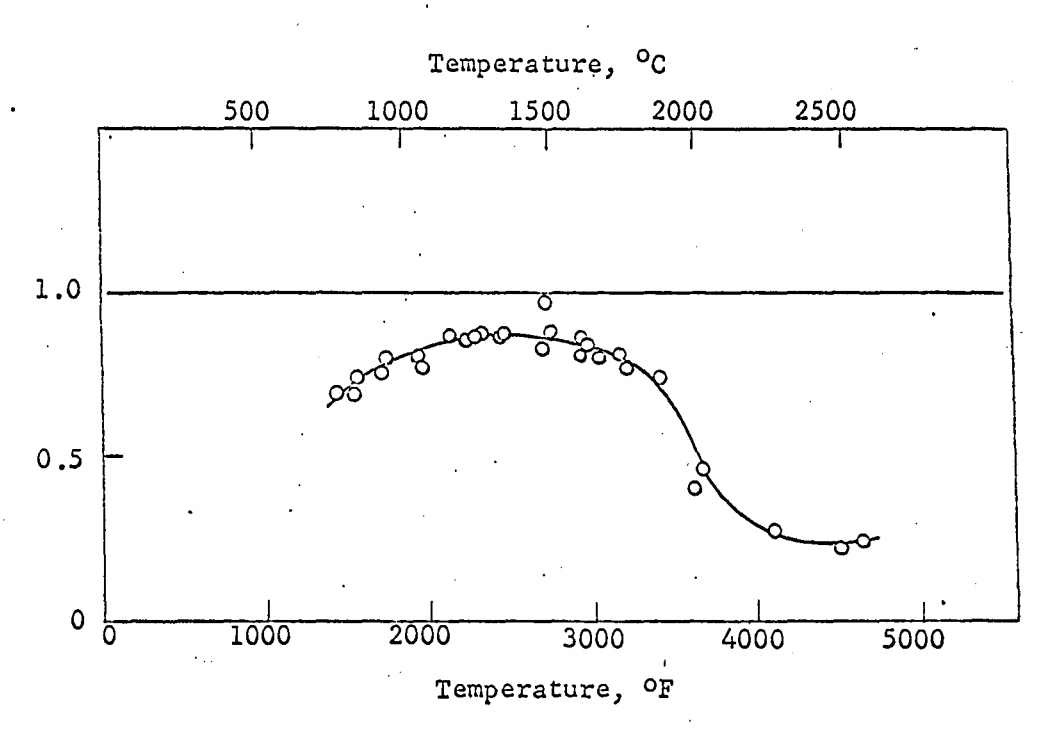


FIGURE 14 - Total Normal Emittance of
Sintered Boride No.6 (Ref. 7)

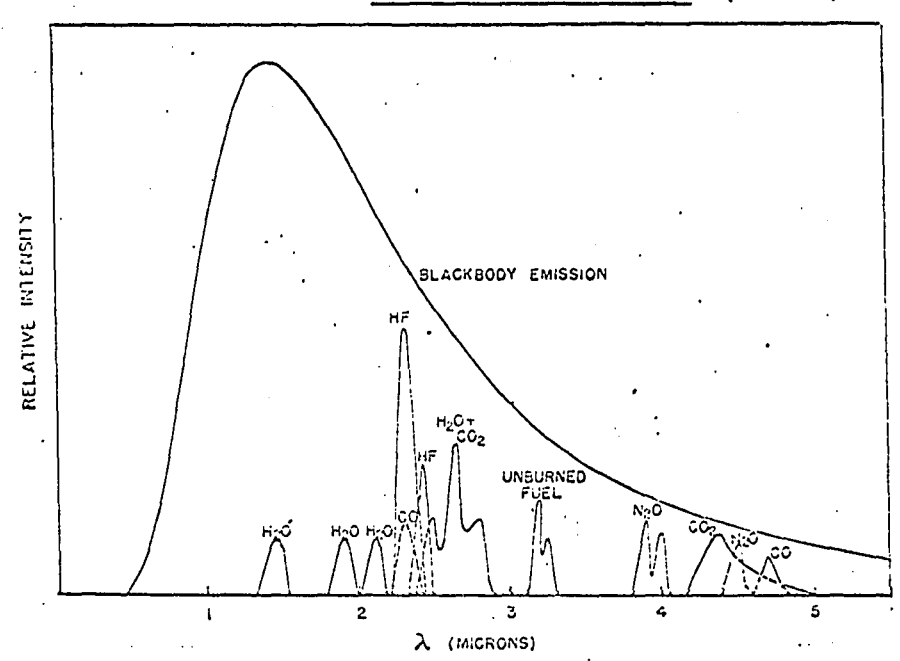


FIGURE 15 - Schematic infrared emission spectra
of typical hot gas molecules
compared to blackbody emission
(References 17-20)

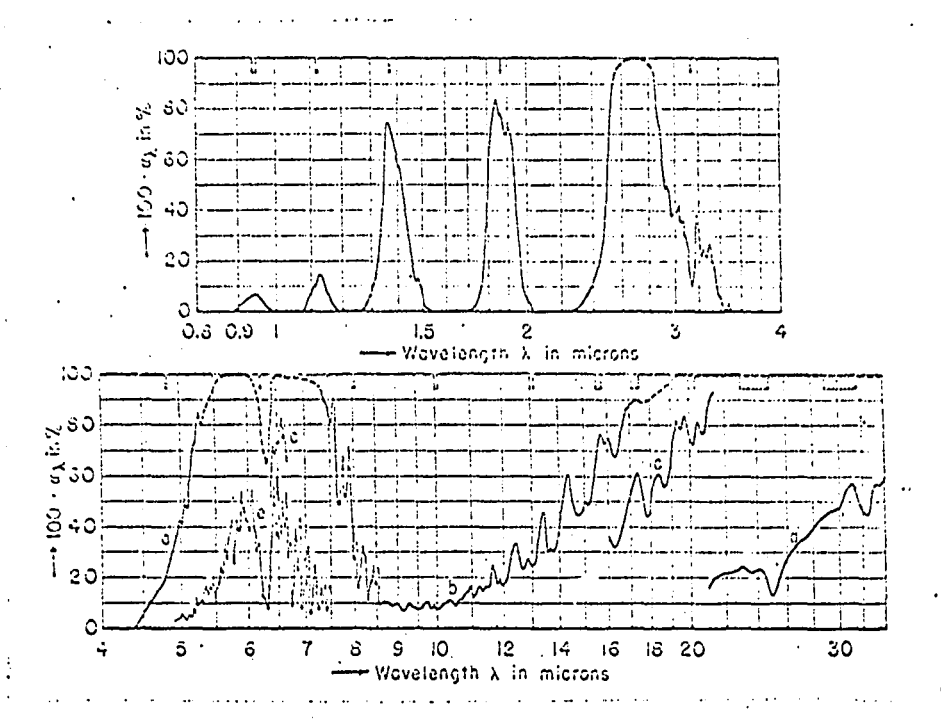


FIGURE 16 - Emission bands of water vapour for various layers
(Ref. 11)

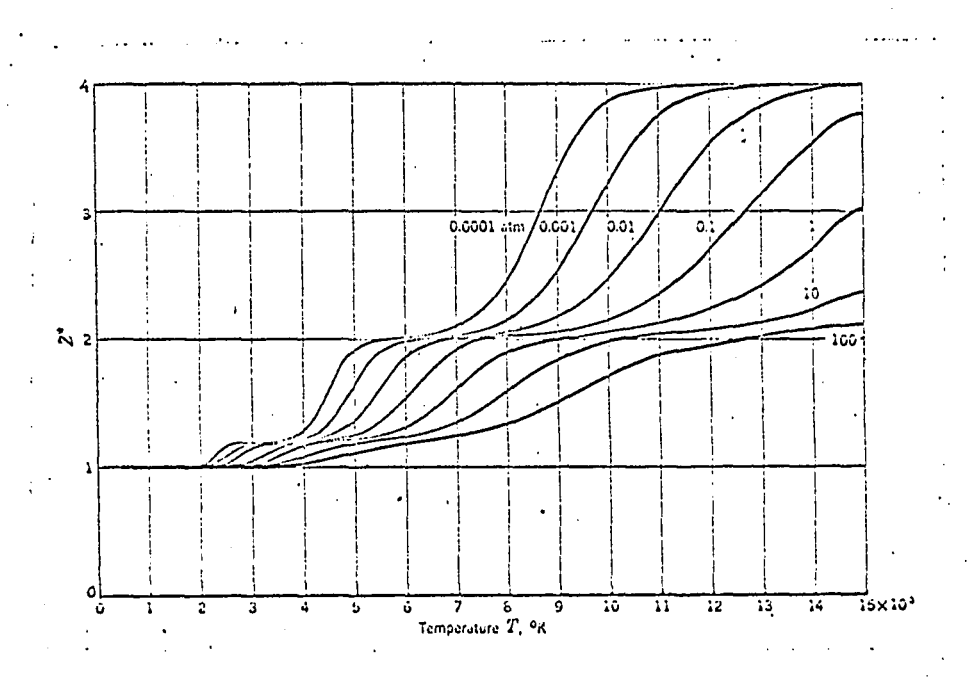


FIGURE 17 - The Factor Z^* for air (Ref. 27)

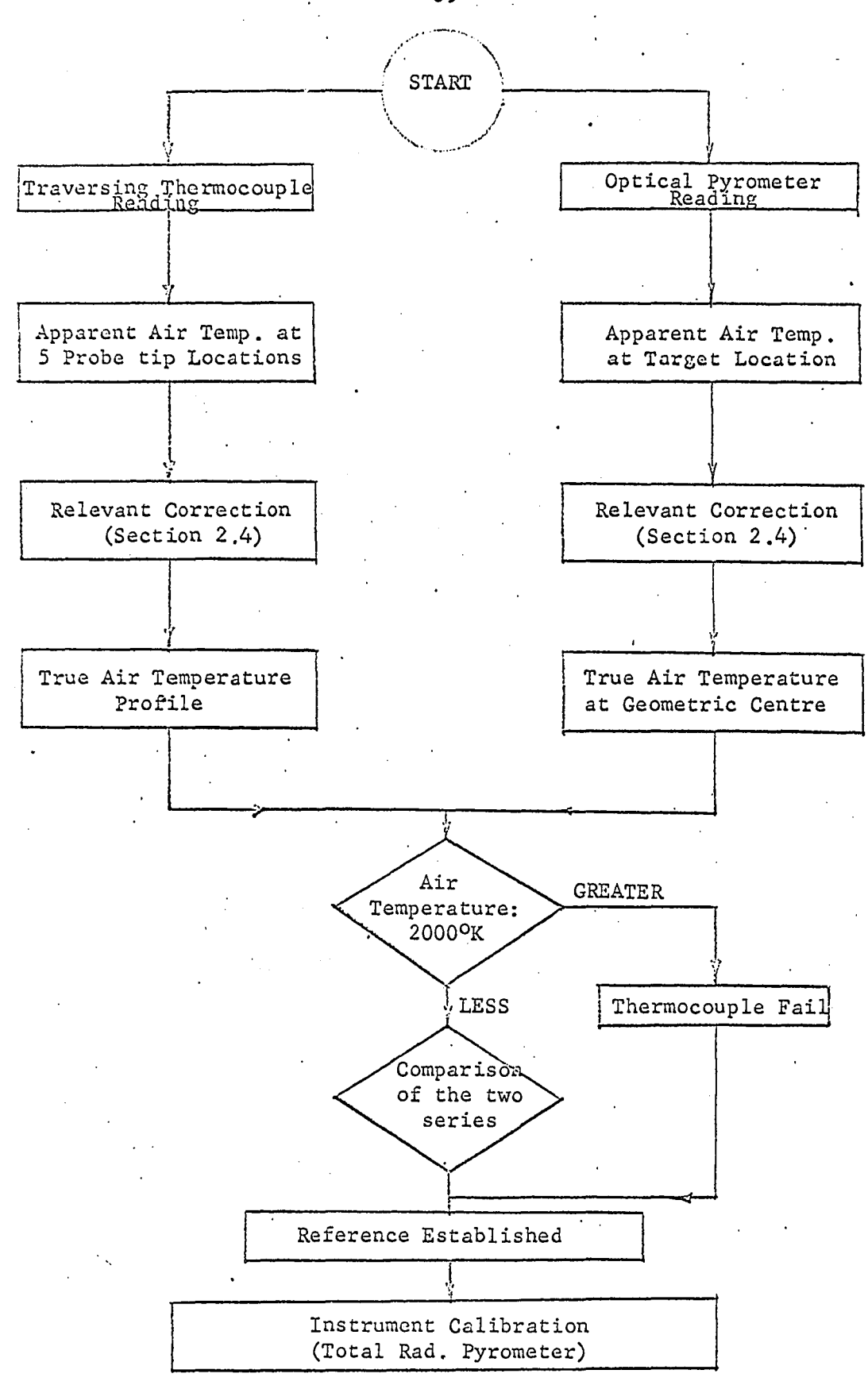
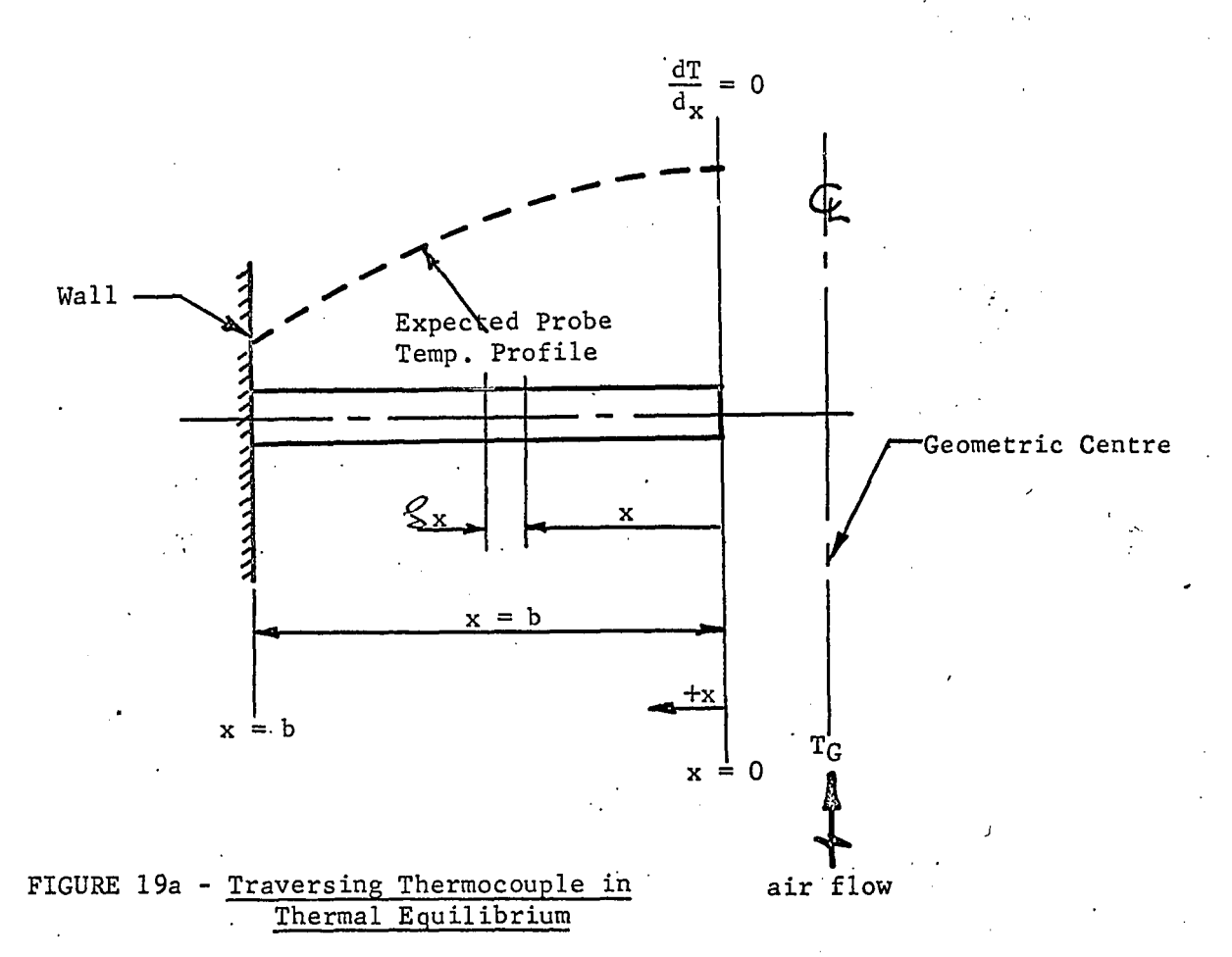


FIGURE 18 - Flow Chart For Procedure Of Air Temperature Determination



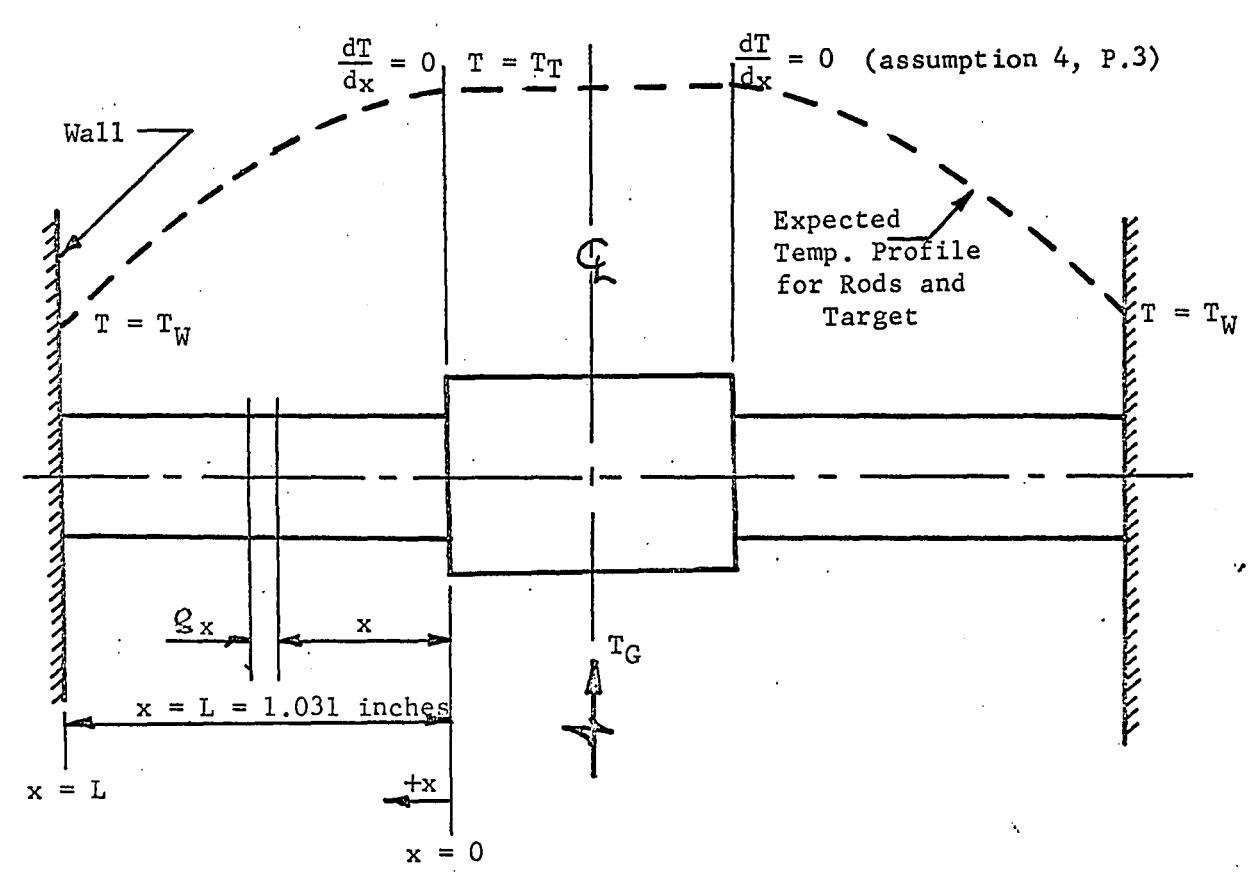


FIGURE 19b - Support Rods in Thermal Equilibrium

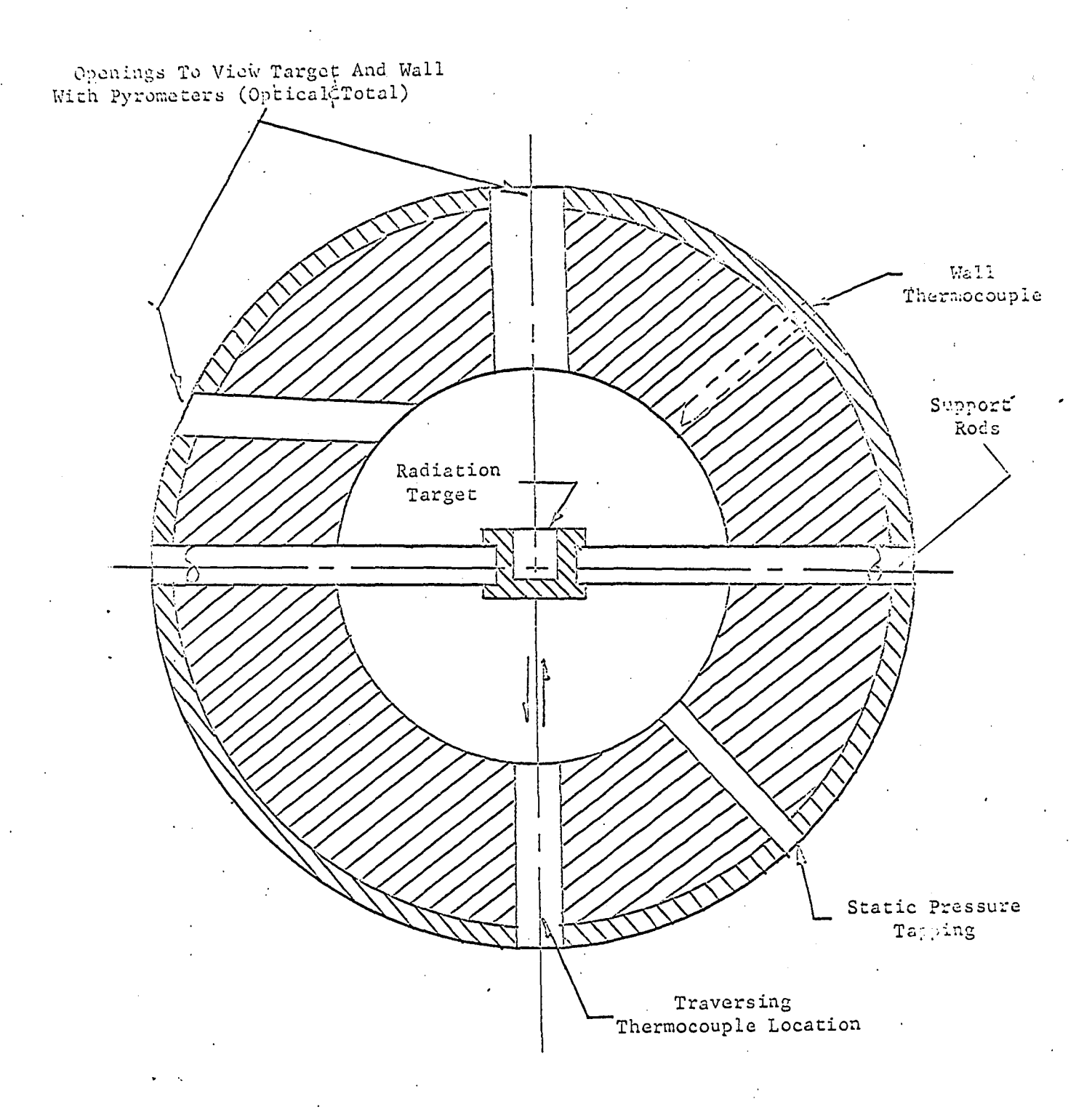


FIGURE 20 - Instrument Locations For Temperature Section

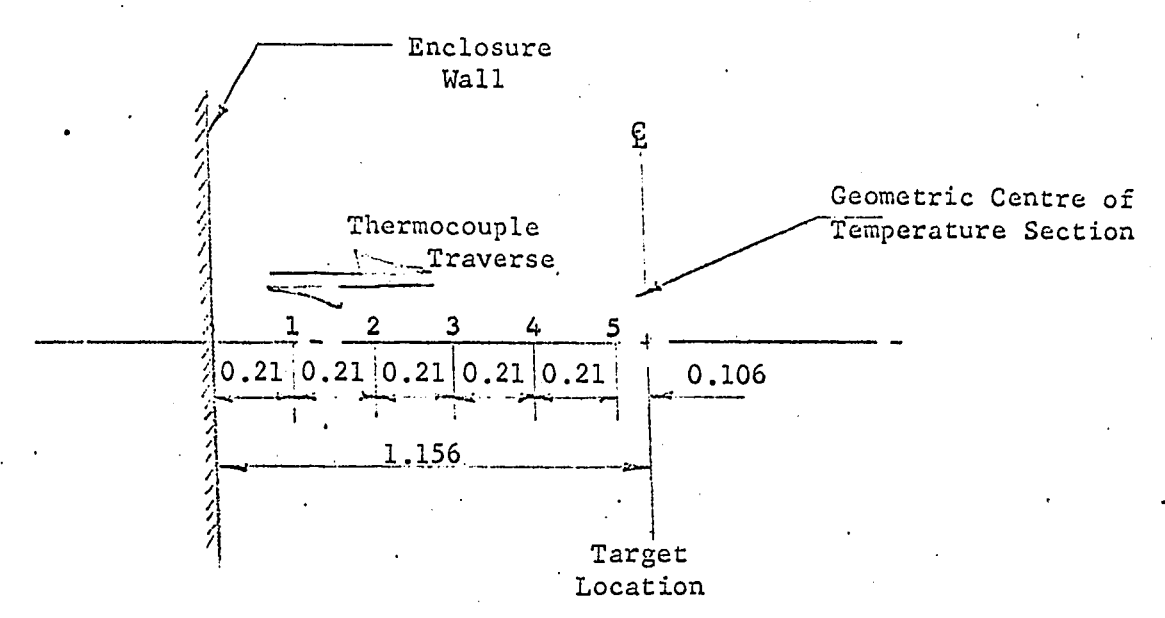


FIGURE 21 - Thermocouple Traverse Locations (Dimensions in inches)

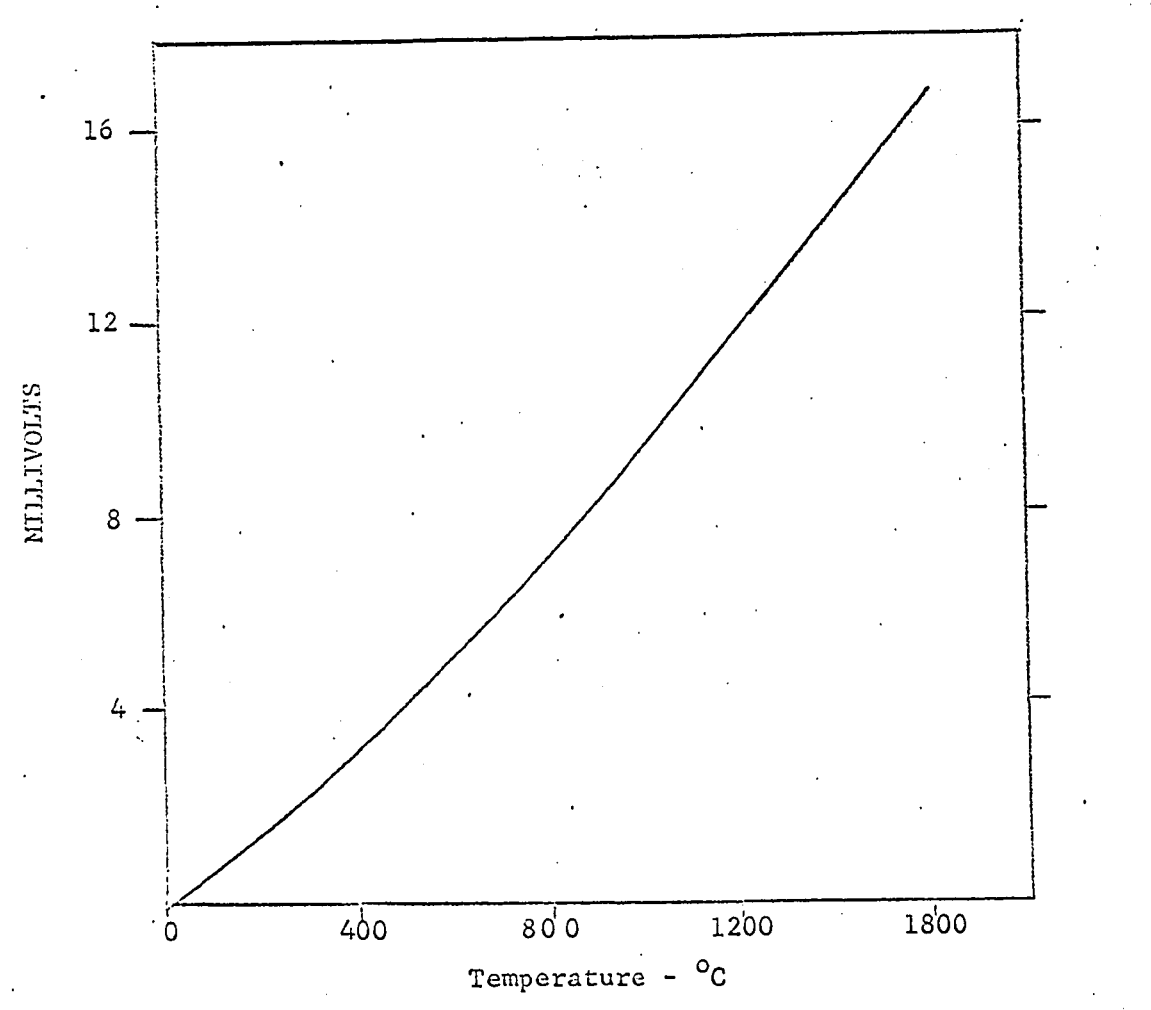


FIGURE 22 - Wall thermocouple Calibration

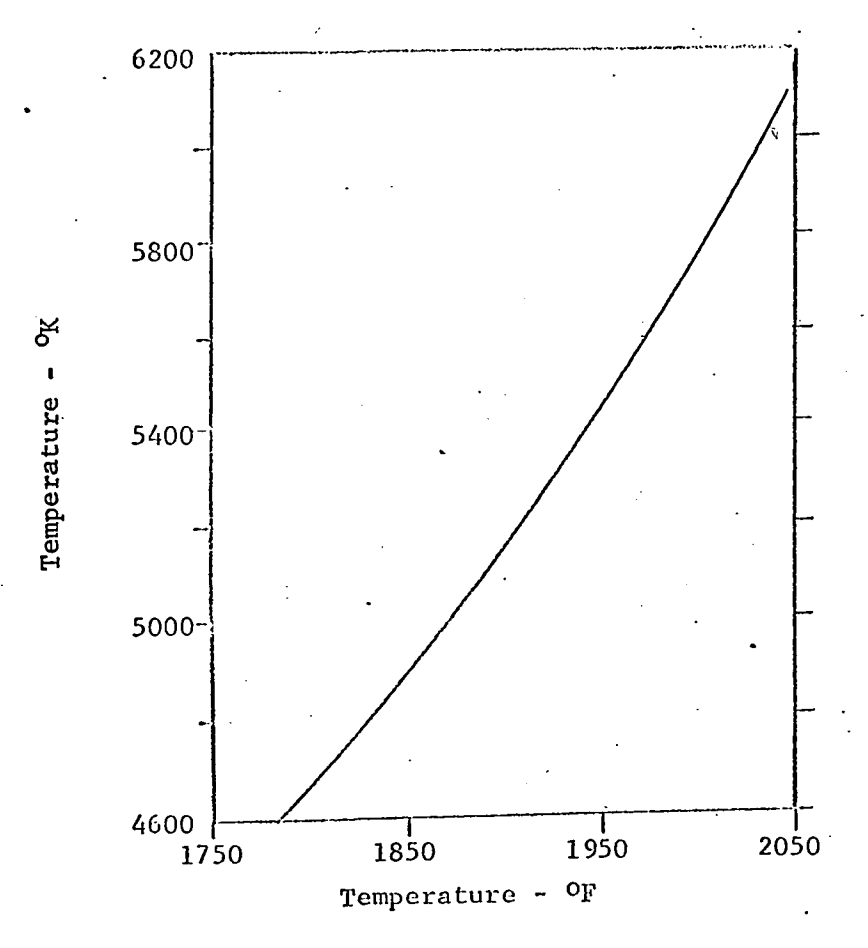


FIGURE 23 - Correction for Range
Extension Screen used
with Optical Pyrometer
(Ref. 40)

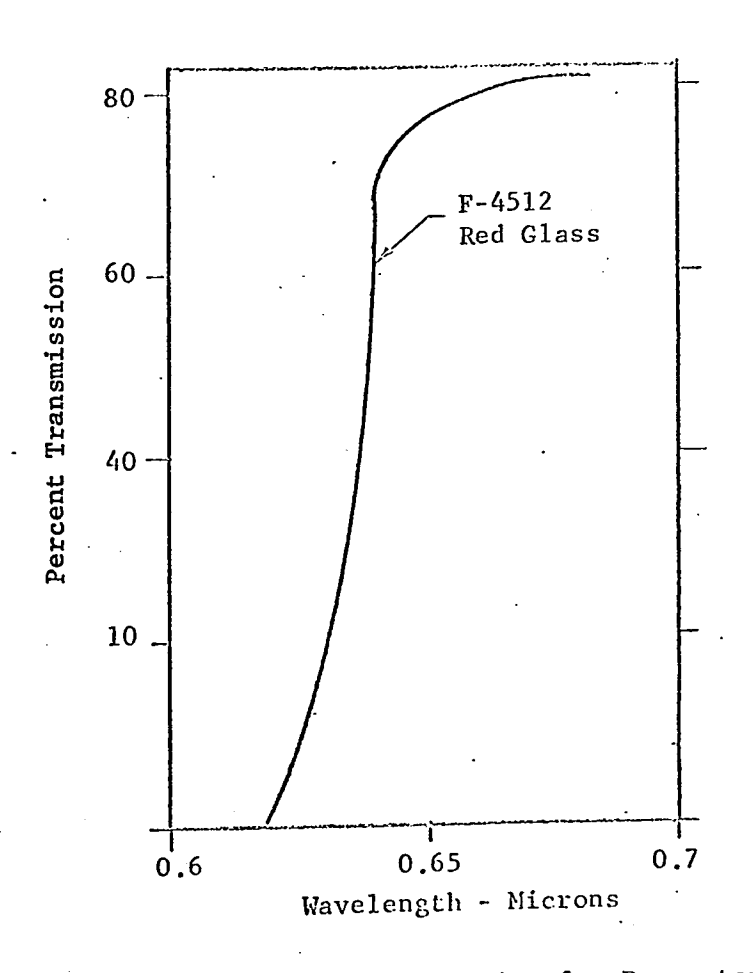
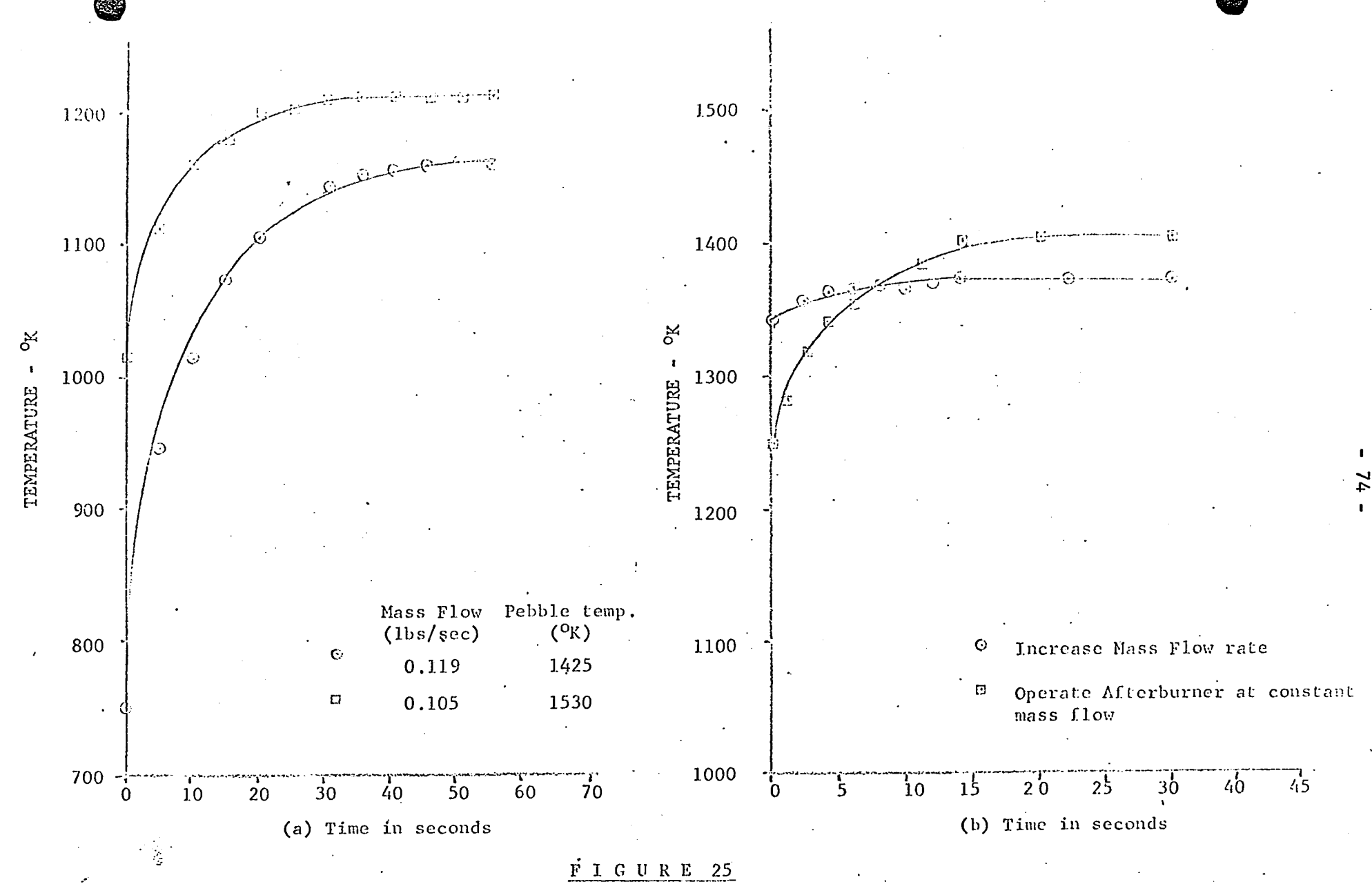


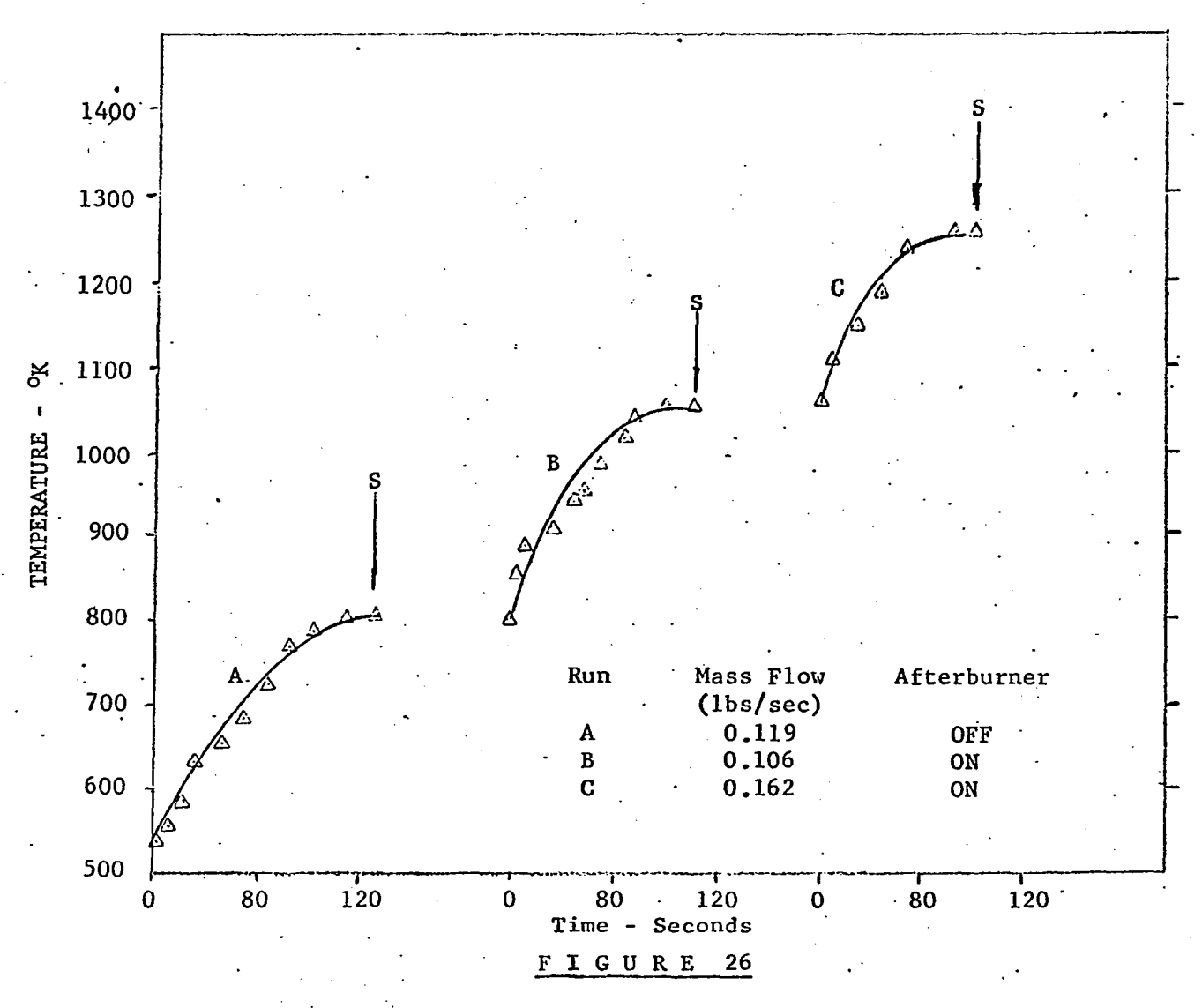
FIGURE 24 - Transmission for Pyrometer Red Glass (Ref. 40)



Traversing Thermocouple Response to Tunnel Operation

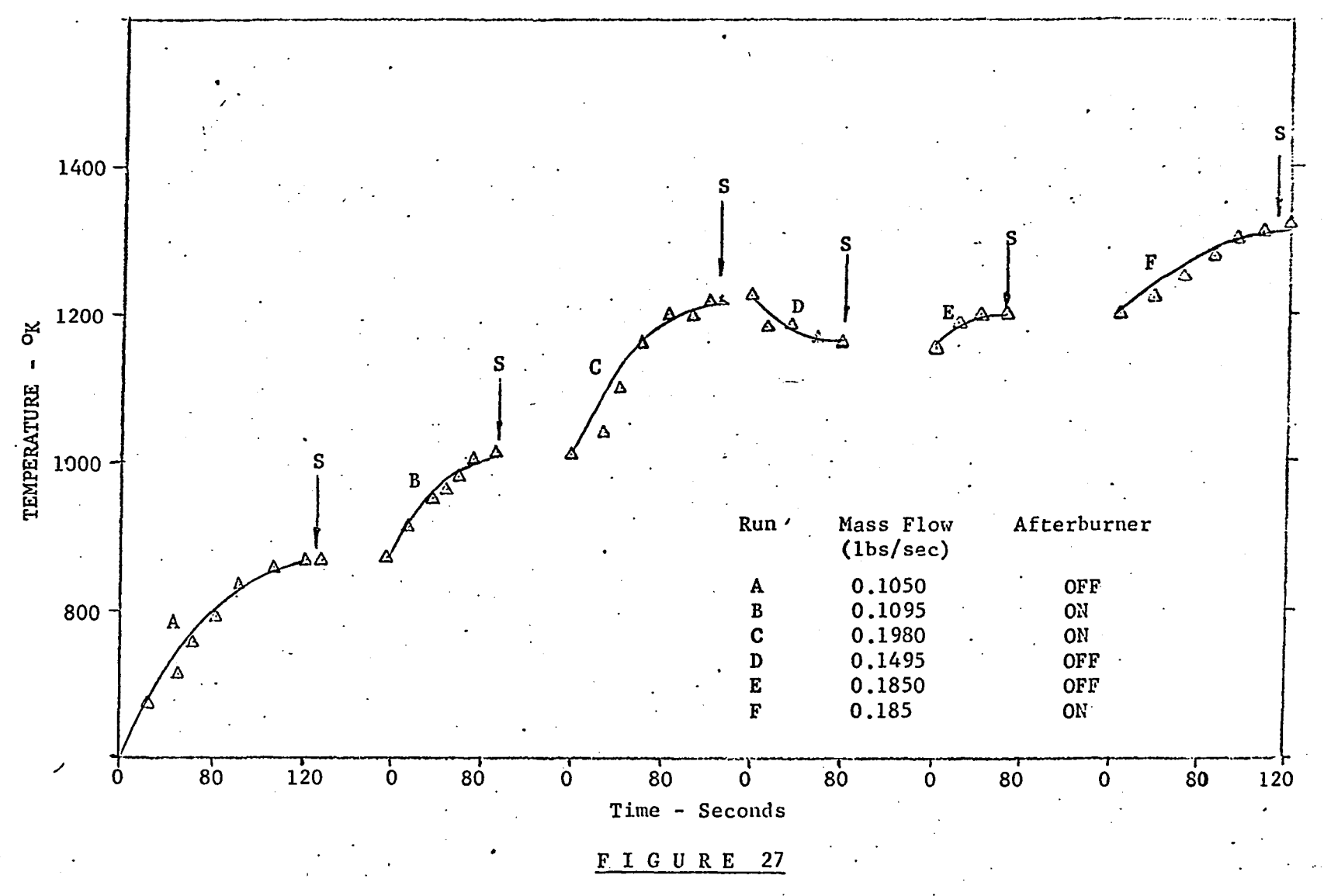
Part (a) each curve indicates the response at the start of blowdown

Part (b) indicates the response as the flow rate is changed or afterburner is operated



Enclosure wall response to tunnel operation

Temperature readings were taken for each run only at steady state i.e. "after S"



Enclosure Wall Response to Tunnel Operation

Temperature readings were taken for each run only at steady state i.e. after "S"

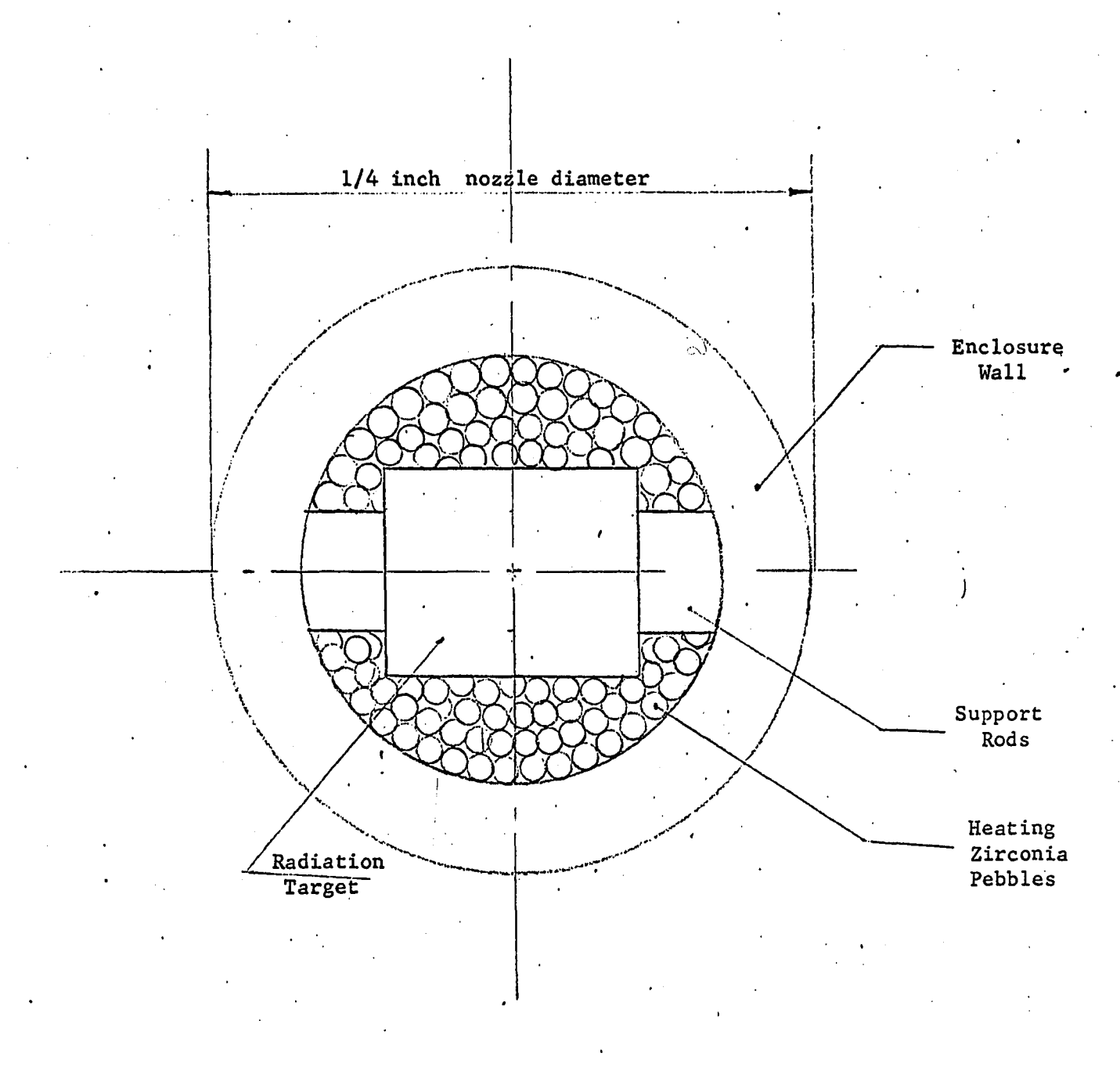
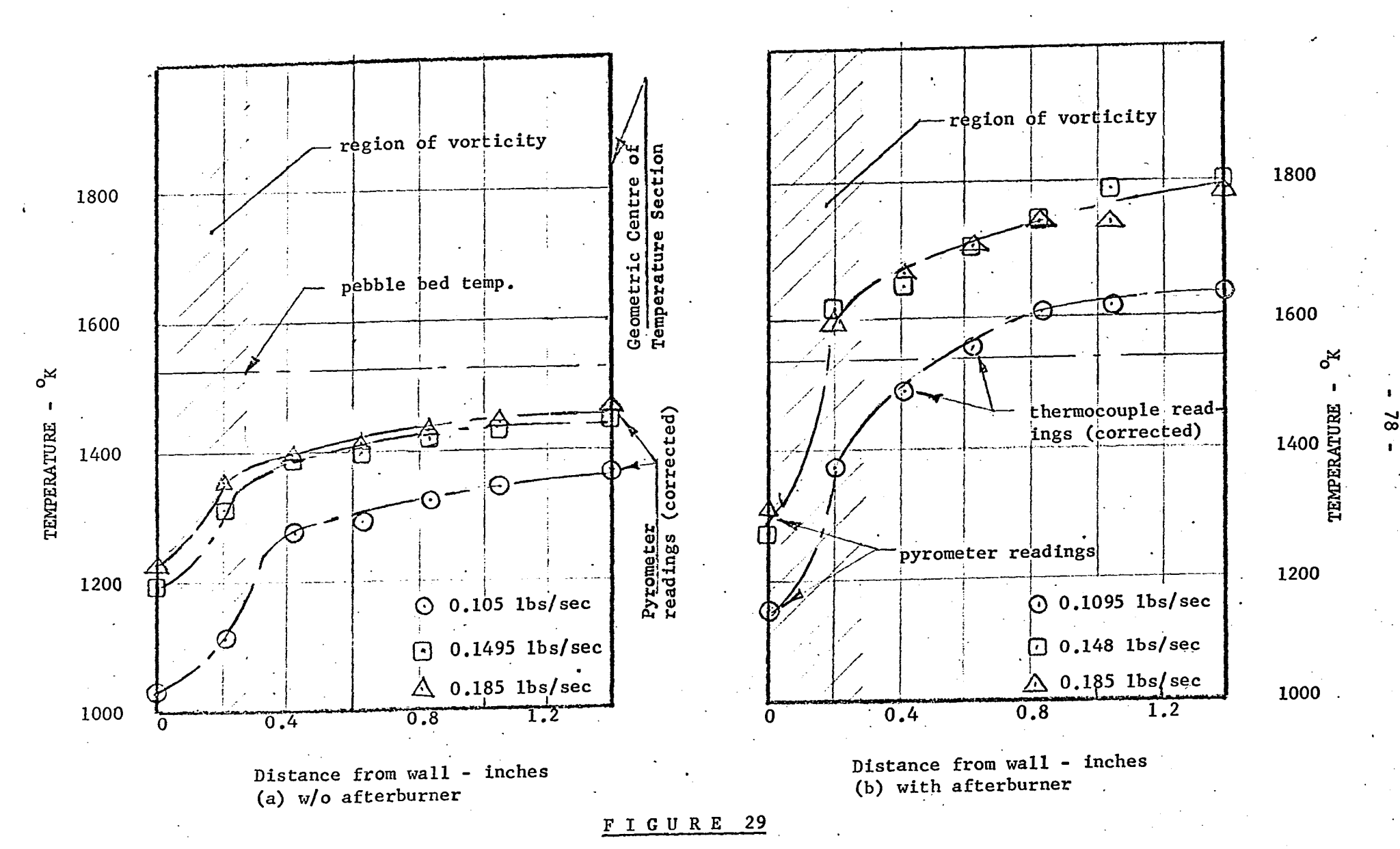
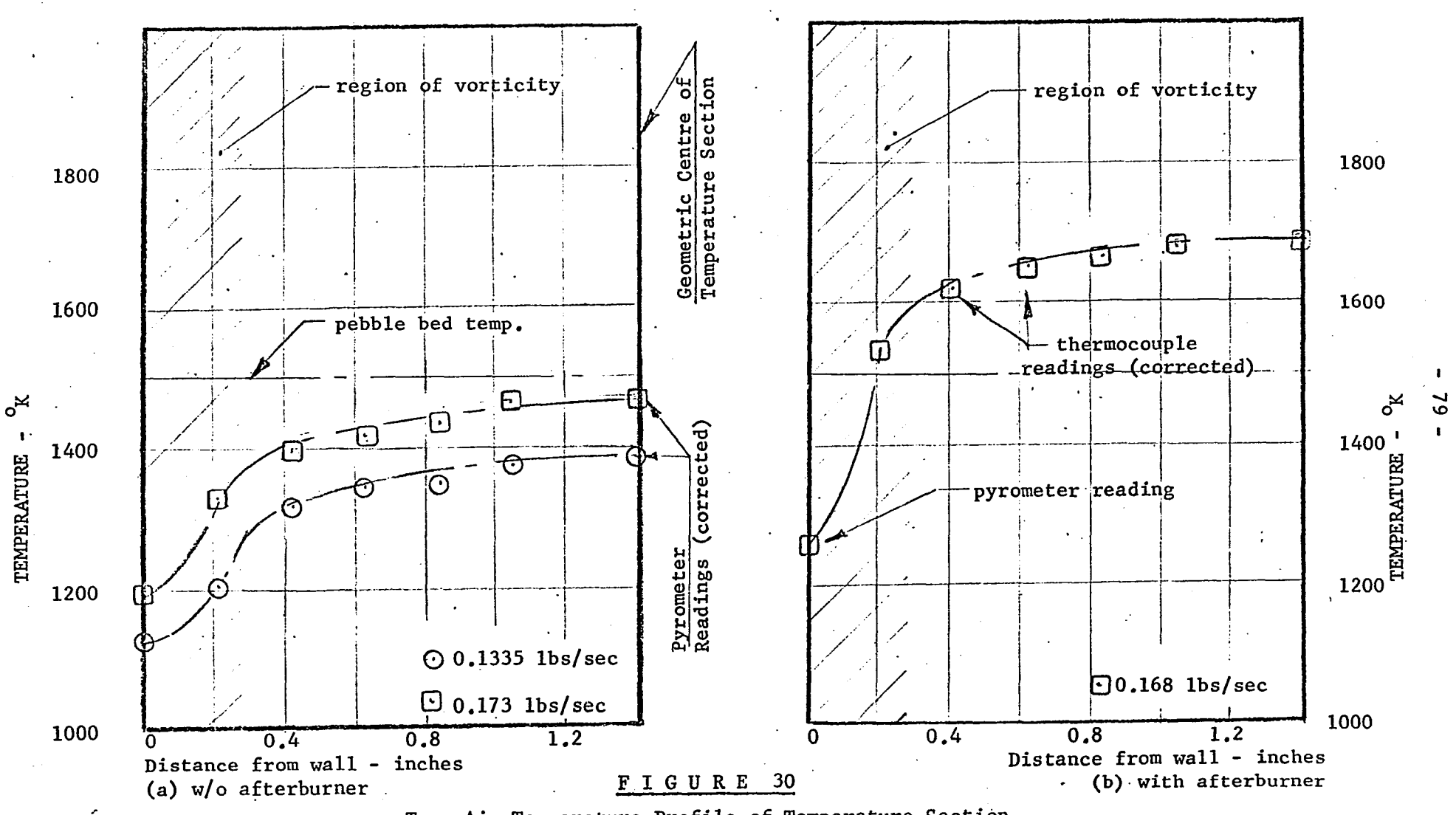


FIGURE 28 - View of pebble bed as seen with optical pyrometer through nozzle



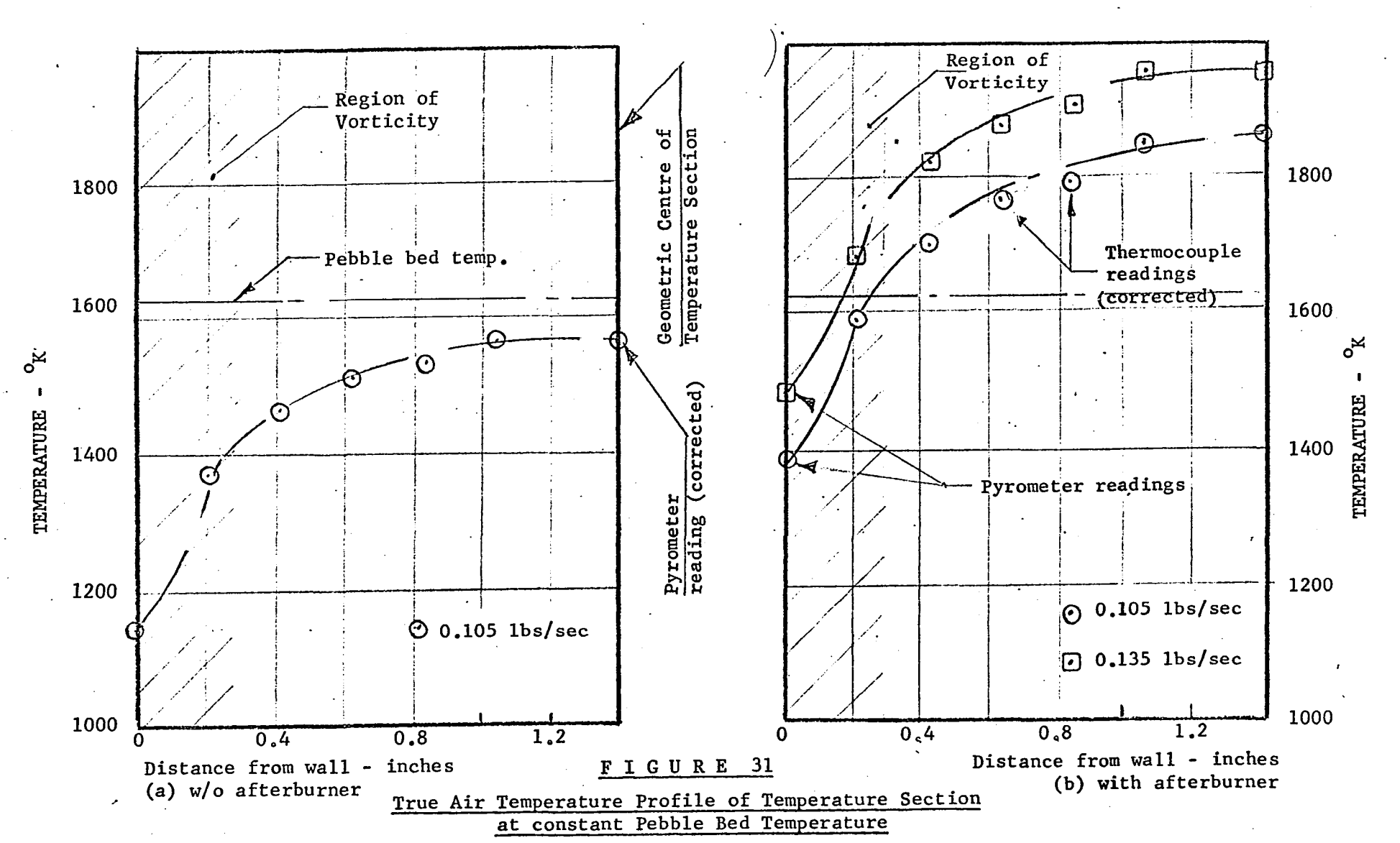
True Air Temperature Profile of Temperature Section at Constant Pebble Bed Temperature

(Note: Curves are drawn only to differentiate between various flow rates)



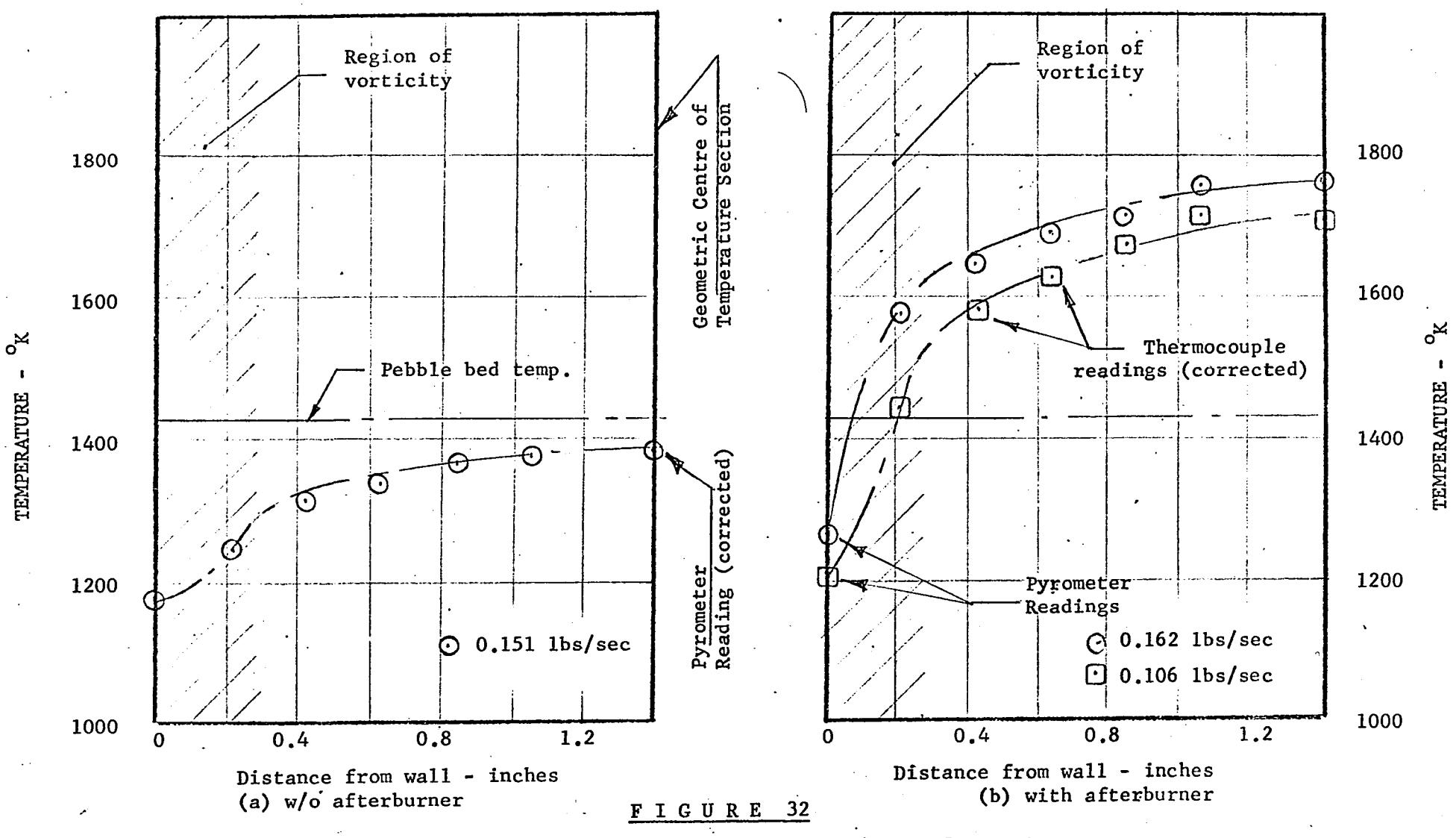
• True Air Temperature Profile of Temperature Section at Constant Pebble Bed Temperatures

(Note: Curves are drawn only to differentiate between various flow rates)



(Note: Curves are drawn only to differentiate between various flow rates)

... 5



True Air Temperature for Temperature Section at Constant

Pebble Bed Temperature

(Note: Curves are drawn only to differentiate between various flow rates)

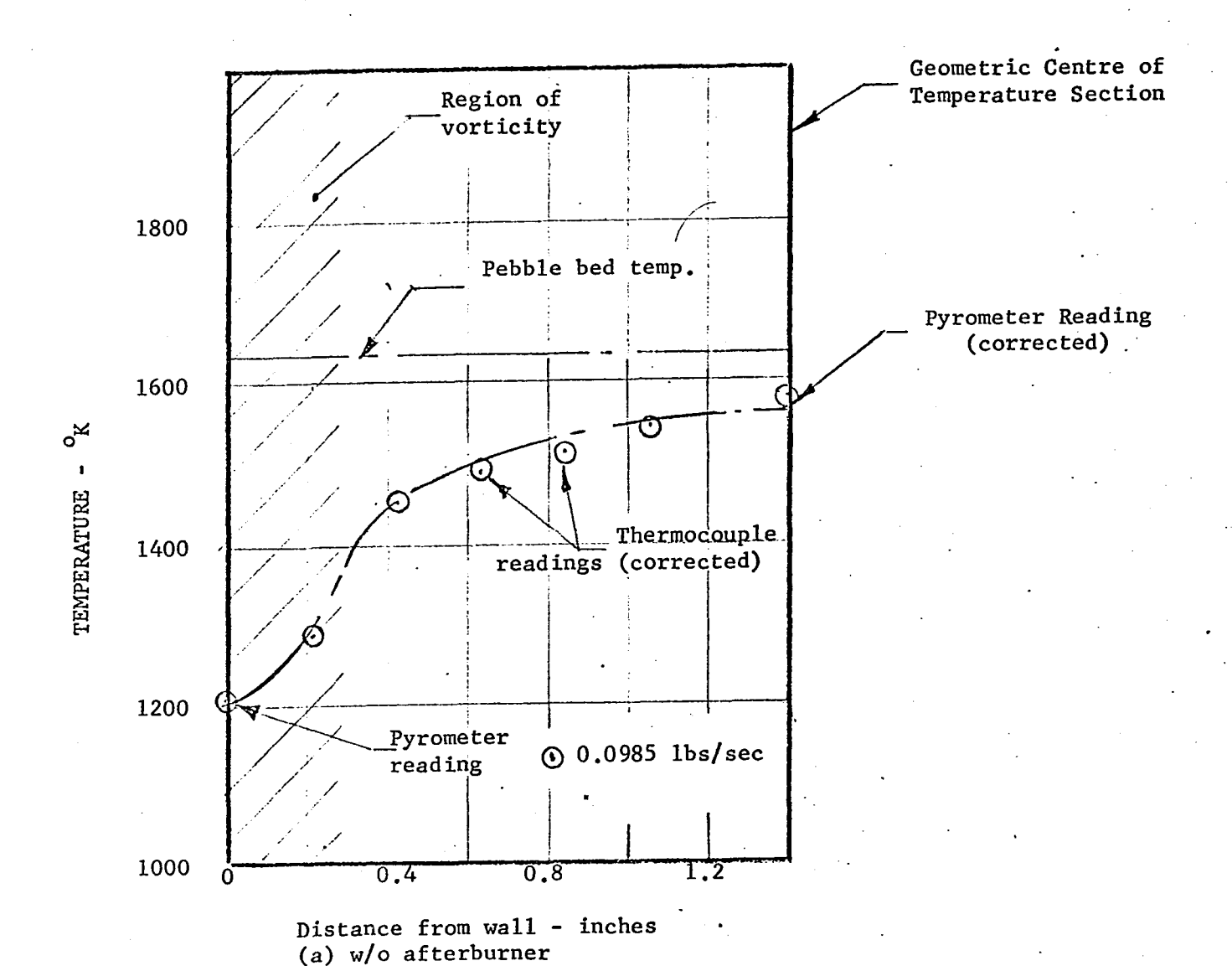
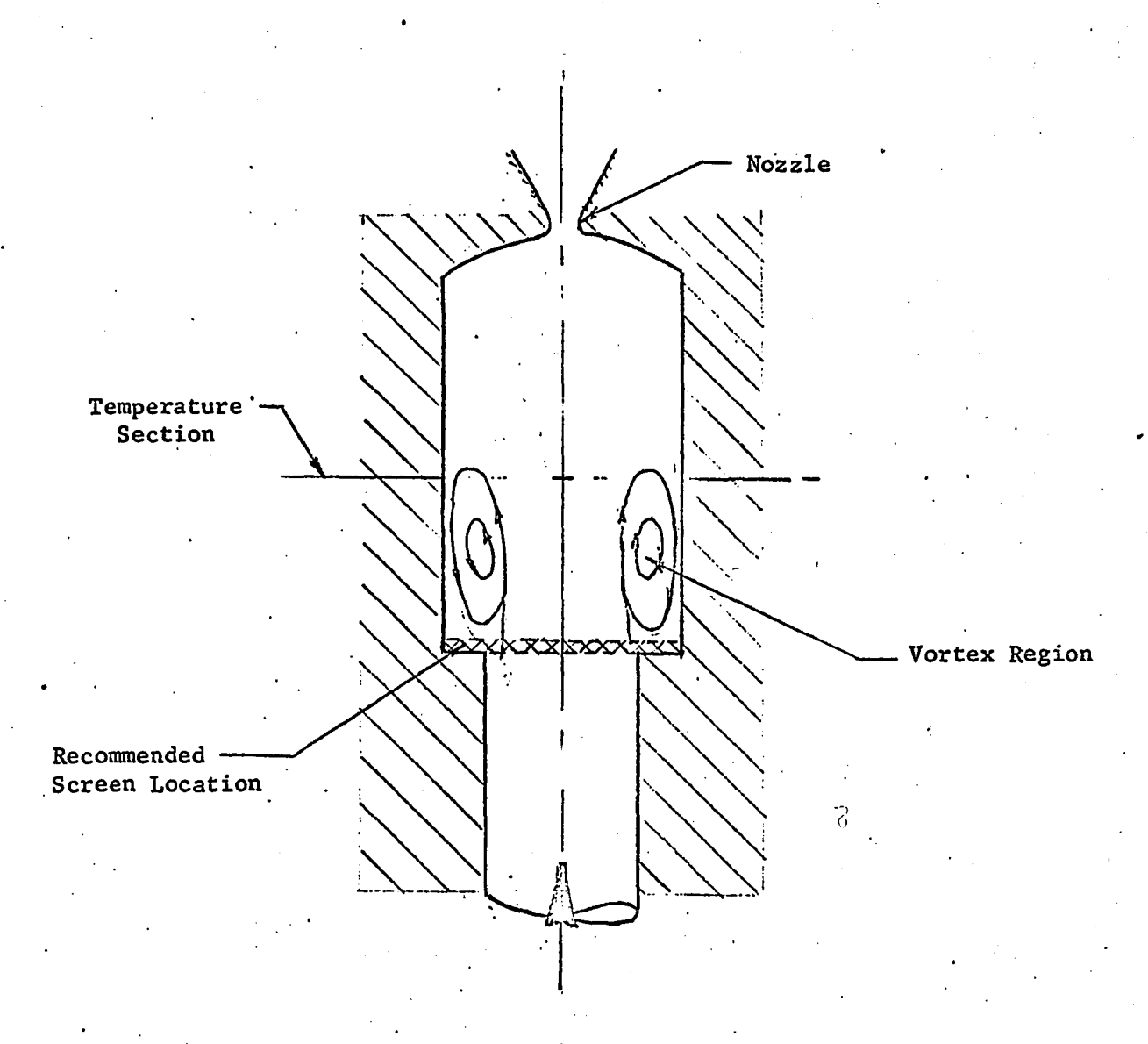


FIGURE 33

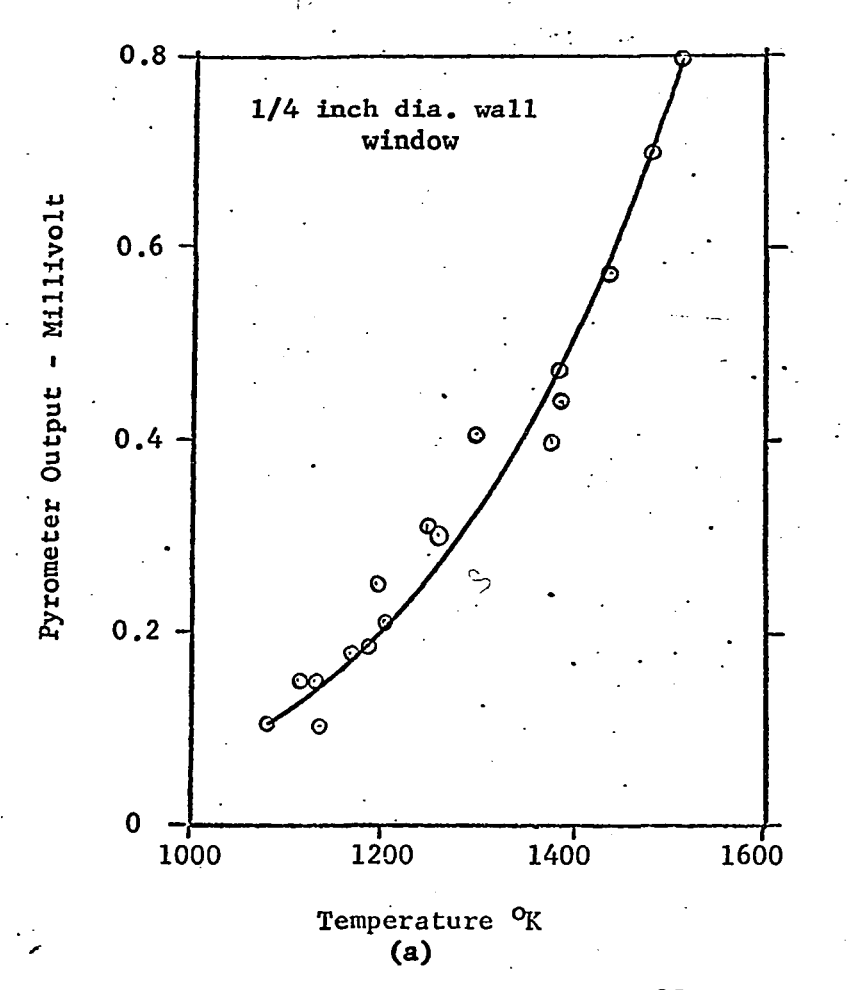
True Air Temperature Profile of Temperature Section
at Constant Pebble Bed Temperature



.Air Flow .

FIGURE 34 - Temperature Section Subject to
A Region of Vorticity





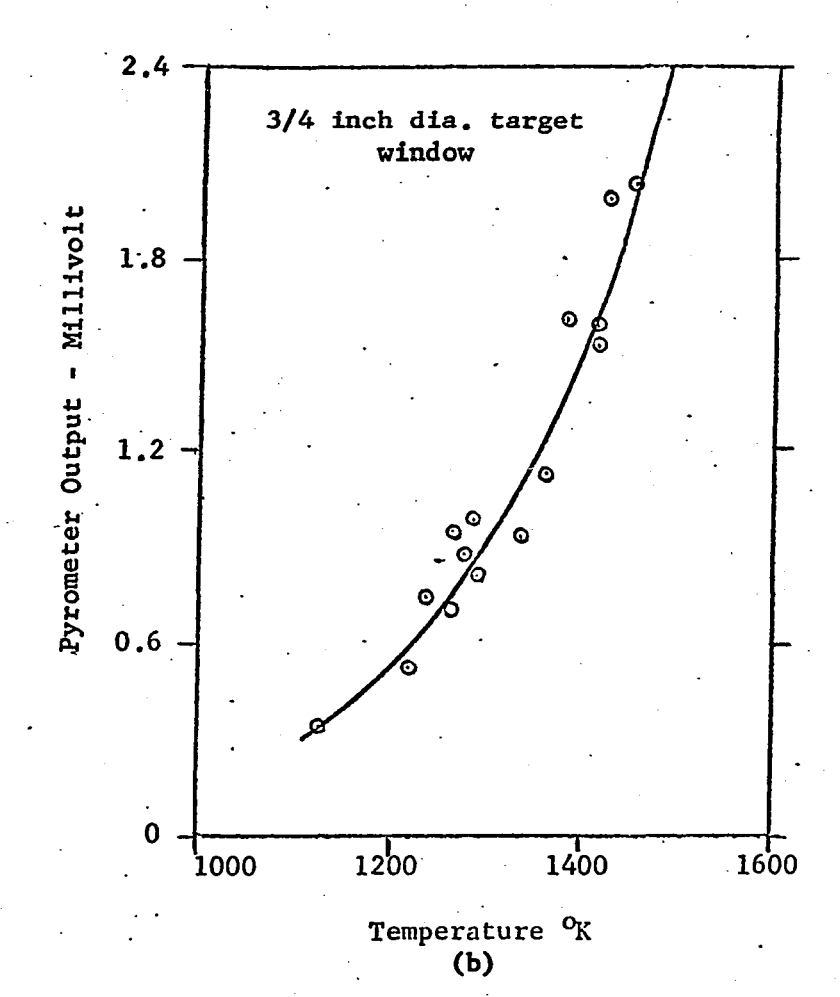


FIGURE 35 - Radiation Pyrometer Output versus temperature for black bodies

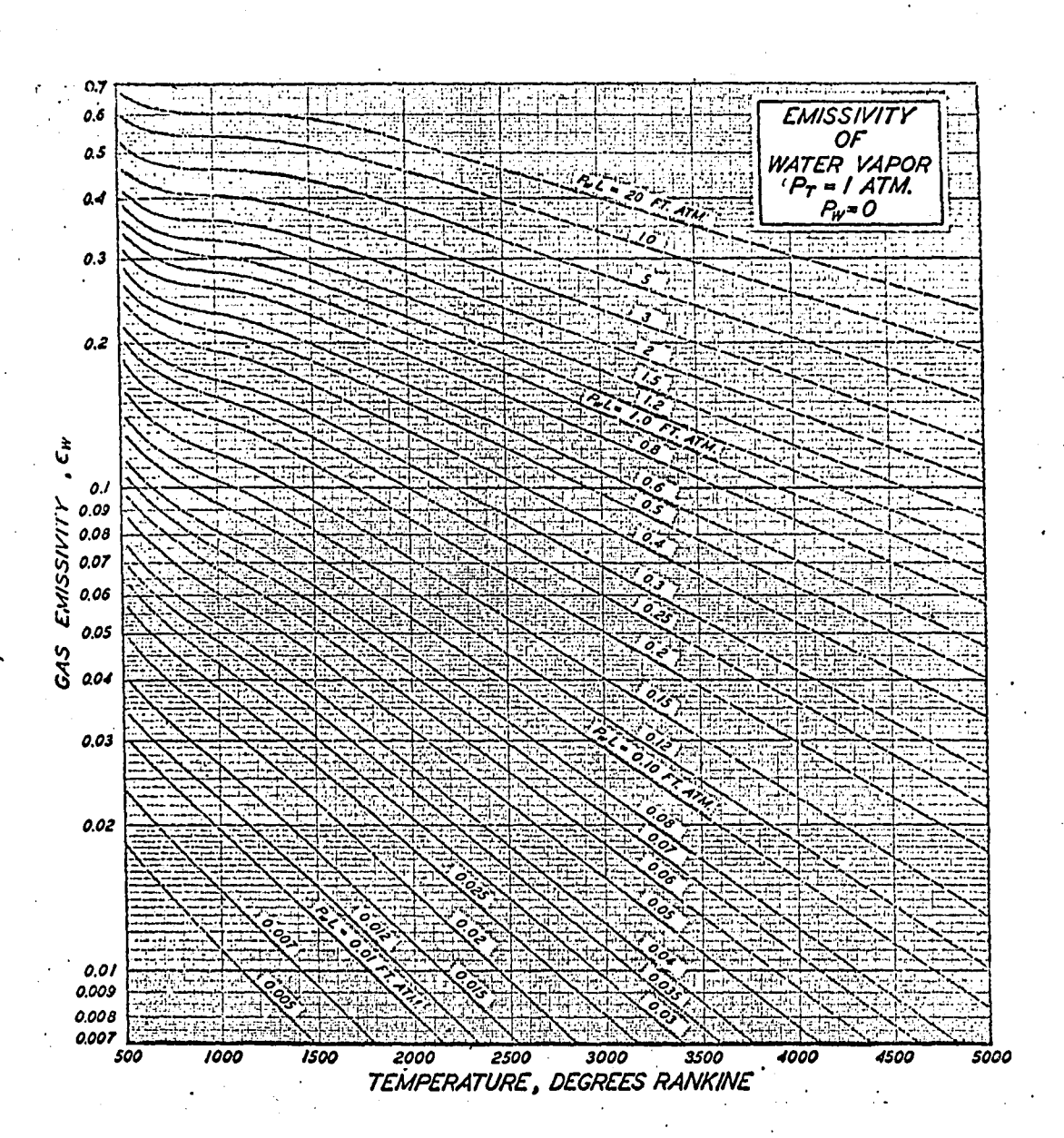


FIGURE 36 - H₂O Vapour Emissivity (Ref. 23)

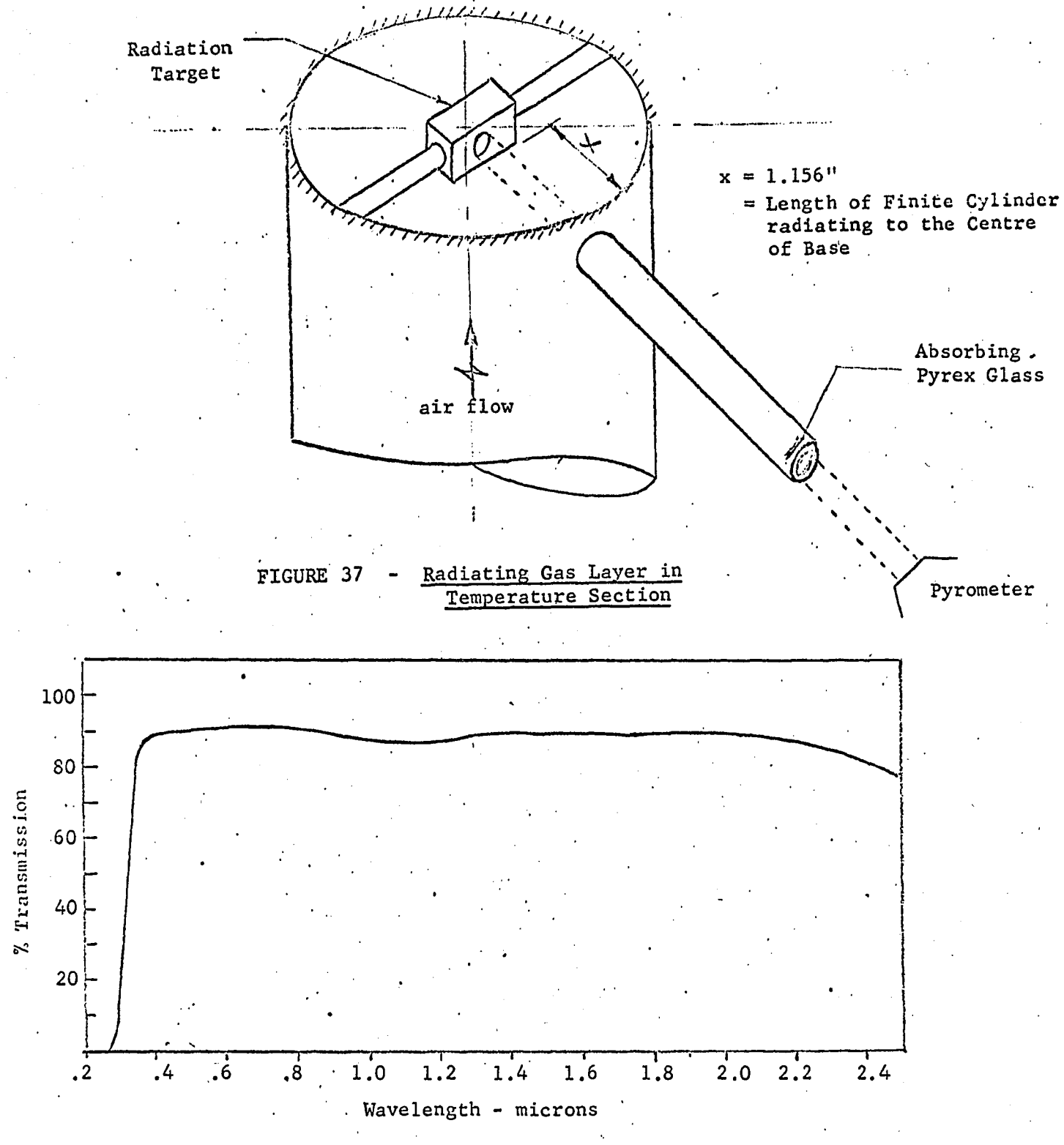


FIGURE 38 - Pyrex Glass (No. 7740) Transmissivity (Ref. 45)

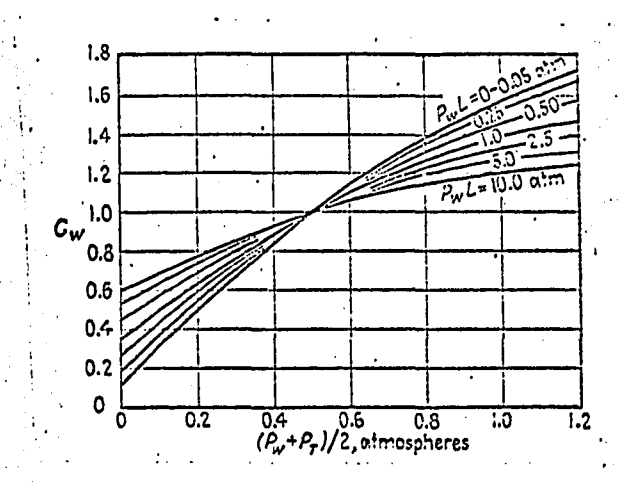


FIGURE 39 - Correction factor $C_{\rm W}$ for converting emissivity of H₂O to values of P_W and P_T other than O and 1 atm, respectively (Ref. 25).